Neurobiology of Disease 132 (2019) 104559

Contents lists available at ScienceDirect

Neurobiology of Disease

journal homepage: www.elsevier.com/locate/ynbdi

Generation of an *Atxn2*-CAG100 knock-in mouse reveals *N*-acetylaspartate production deficit due to early *Nat8l* dysregulation

Nesli-Ece Sen[a,1], Júlia Canet-Pons[a,1], Melanie V. Halbach[a,1], Aleksandar Arsovic[a], Ulrich Pilatus[b], Woon-Hyung Chae[c], Zeynep-Ece Kaya[a,d], Kay Seidel[e], Ewa Rollmann[a], Michel Mittelbronn[f,g,h,i,j], David Meierhofer[k], Chris I. De Zeeuw[l,m], Laurens W.J. Bosman[m], Suzana Gispert[a], Georg Auburger[a,*]

[a] *Experimental Neurology, Goethe University Medical School, 60590 Frankfurt am Main, Germany*
[b] *Institute of Neuroradiology, Goethe University Medical School, 60590 Frankfurt am Main, Germany*
[c] *Georg-Speyer-Haus, Institute for Tumor Biology and Experimental Therapy, 60596 Frankfurt am Main, Germany*
[d] *Department of Neurology, Cerrahpasa School of Medicine, Istanbul University, 34098 Istanbul, Turkey*
[e] *Department of Anatomy II, Institute of Clinical Neuroanatomy, Goethe University, 60590 Frankfurt am Main, Germany*
[f] *Neurological Institute (Edinger Institute), Goethe University, 60590 Frankfurt am Main, Germany*
[g] *Luxembourg Centre of Neuropathology (LCNP), Luxembourg*
[h] *Department of Pathology, Laboratoire National de Santé (LNS), Dudelange, Luxembourg*
[i] *Luxembourg Centre for Systems Biomedicine (LCSB), University of Luxembourg, Esch-sur-Alzette, Luxembourg*
[j] *Department of Oncology, NORLUX Neuro-Oncology Laboratory, Luxembourg Institute of Health (LIH), Luxembourg*
[k] *Max Planck Institute for Molecular Genetics, 14195 Berlin, Germany*
[l] *Netherlands Institute for Neuroscience, Royal Academy of Arts and Sciences, 1105 BA Amsterdam, the Netherlands*
[m] *Department of Neuroscience, Erasmus Medical Center, 3000 CA Rotterdam, the Netherlands*

ARTICLE INFO

Keywords:
N-acetylaspartate
Molecular biomarkers of disease
Polyglutamine expansion
Stress granules
Mitochondrial bioenergetics
RNA processing

ABSTRACT

Spinocerebellar ataxia type 2 (SCA2) is an autosomal dominant neurodegenerative disorder caused by CAG-expansion mutations in the *ATXN2* gene, mainly affecting motor neurons in the spinal cord and Purkinje neurons in the cerebellum. While the large expansions were shown to cause SCA2, the intermediate length expansions lead to increased risk for several atrophic processes including amyotrophic lateral sclerosis and Parkinson variants, e.g. progressive supranuclear palsy. Intense efforts to pioneer a neuroprotective therapy for SCA2 require longitudinal monitoring of patients and identification of crucial molecular pathways. The ataxin-2 (ATXN2) protein is mainly involved in RNA translation control and regulation of nutrient metabolism during stress periods. The preferential mRNA targets of ATXN2 are yet to be determined. In order to understand the molecular disease mechanism throughout different prognostic stages, we generated an *Atxn2*-CAG100-knock-in (KIN) mouse model of SCA2 with intact murine ATXN2 expression regulation. Its characterization revealed somatic mosaicism of the expansion, with shortened lifespan, a progressive spatio-temporal pattern of pathology with subsequent phenotypes, and anomalies of brain metabolites such as *N*-acetylaspartate (NAA), all of which mirror faithfully the findings in SCA2 patients. Novel molecular analyses from stages before the onset of motor deficits revealed a strong selective effect of ATXN2 on *Nat8l* mRNA which encodes the enzyme responsible for NAA synthesis. This metabolite is a prominent energy store of the brain and a well-established marker for neuronal health. Overall, we present a novel authentic rodent model of SCA2, where in vivo magnetic resonance imaging was feasible to monitor progression and where the definition of earliest transcriptional abnormalities was possible. We believe that this model will not only reveal crucial insights regarding the pathomechanism of SCA2 and other ATXN2-associated disorders, but will also aid in developing gene-targeted therapies and disease prevention.

* Corresponding author.
E-mail address: auburger@em.uni-frankfurt.de (G. Auburger).
[1] Joint first authors.

https://doi.org/10.1016/j.nbd.2019.104559
Received 29 May 2019; Received in revised form 16 July 2019; Accepted 30 July 2019
Available online 31 July 2019

1. Introduction

Spinocerebellar ataxia type 2 (SCA2) is an autosomal dominantly inherited neurodegenerative disorder mainly affecting Purkinje cells in the cerebellum and motor neurons in the spinal cord (Auburger et al., 2017). Patients suffer from uncoordinated movement, gait ataxia, dysarthria, and intention tremor. Before the development of ataxia, already a slowing of ocular saccade movements and an increase of muscle cramps appear. In the nervous system, the typical multi-system atrophy progresses over 25 years (Antenora et al., 2018), until patients die from respiratory failure due to motor neuron loss (Lastres-Becker et al., 2008b). In peripheral tissues, atrophy of muscle mass and body fat are prominent at the late immobility stage (Velazquez-Perez et al., 2017b), but it is noteworthy that subcutaneous fat tissue loss appears in craniocervical distribution already at presymptomatic stages. Monitoring the disease progression and assessing therapeutic benefits is aided by the identification of biomarkers that are easily quantified in living patients. A prominent metabolite in brain that is generated by neuronal mitochondria and used in oligodendroglia for myelinogenesis, *N*-acetylaspartate (NAA), can be detected by magnetic resonance imaging (MRI) spectroscopy. It shows reduced levels in SCA2, and in various other progressive neurodegenerative disorders as well as in brain injury (Guerrini et al., 2004). The extent of NAA decrease was found highly correlated with the progression of SCA2 (Cahill Jr. and Veech, 2003; Wang et al., 2012).

Dynamic CAG-repeat expansion mutations in *ATXN2* gene have been identified as the monogenic cause of SCA2. While healthy individuals have 22 repeat units in the first exon of *ATXN2,* encoding a domain with 22 glutamine (Glu, Q) amino acids, SCA2 patients have > 33 repeat units in this region (Auburger et al., 1990; Orozco Diaz et al., 1990; Pulst et al., 1996). Larger repeat expansions lead to earlier disease onset, faster progression, more widespread pathology and earlier death (Almaguer-Mederos et al., 2013; Almaguer-Mederos et al., 2010; Rub et al., 2013; Tuin et al., 2006; Velazquez-Perez et al., 2009; Velazquez-Perez et al., 2004). For instance, patients with 92 and 116 repeat units had clinical manifestation within the first year of life and showed multi-system atrophy of cerebellum, brainstem and cerebrum (Di Fabio et al., 2012; Vinther-Jensen et al., 2013). Aside from the repeat size, the structure of the repeat region also differs between patients and healthy individuals; the normal *ATXN2* allele contains 22 repeats with CAA interruptions in the form of $(CAG)_8CAA(CAG)_4CAA(CAG)_8$. Interestingly, most SCA2 patients lack both CAA units and have pure CAG-repeats instead. As CAA and CAG both code for glutamine, the protein structure remains the same, however instability of a pure CAG-repeat region at DNA level is significantly higher and leads to even larger expansions in the following generations. Intermediate-length expansions of 26–30 repeats with CAA interruptions have been shown to increase the risk of developing motor neuron diseases like ALS (Amyotrophic Lateral Sclerosis) or FTLD (Fronto-Temporal Lobar Dementia) (Elden et al., 2010; Gispert et al., 2012; Lee et al., 2011). Also, a specific haplotype of single nucleotide polymorphisms in *ATXN2* is associated with higher risk of ALS (Lahut et al., 2012). In addition, pathogenic *ATXN2* expansions with CAA interruptions were reported to underlie dopaminergic midbrain neuron atrophy in families with Parkinson's disease (PD) (Gispert et al., 2012; Park et al., 2015).

Ataxin-2 (ATXN2) is an evolutionarily conserved protein in the eukaryotes, associated with mRNA translational regulation and stress response. Under normal conditions, ATXN2 is located in the cytosol, partly associated with the ribosomal machinery at the endoplasmic reticulum (ER), where it modulates protein synthesis (Fittschen et al., 2015; Fleischer et al., 2006; van de Loo et al., 2009). Upon cell damage or bioenergetic deficits, its transcription is enhanced and ATXN2 relocalizes to stress granules (SGs) where mRNAs are stalled to undergo quality control until protein synthesis is resumed after stress (Heck et al., 2014; Kedersha et al., 2013; Lastres-Becker et al., 2016; Nonhoff et al., 2007). Interaction of ATXN2 with mRNAs occur either directly via its N-terminal Lsm and LsmAD domains, or indirectly through interaction with Poly(A) Binding Protein (PABP) via its C-terminal PAM2 motif. ATXN2 also contains several proline-rich motifs interspersed throughout the protein that modulate trophic receptor endocytosis and growth pathways (Auburger et al., 2017; Drost et al., 2013; Lastres-Becker et al., 2008a; Nonis et al., 2008; Lastres-Becker, 2019). It is unclear if ATXN2 binds to many or few RNAs, but its impact on neuronal habituation via specific microRNA interaction and on the circadian rhythm via *Per* mRNA interaction have been reported (Pfeffer et al., 2017; Sudhakaran et al., 2014). Through interaction with specific proteins like TDP-43 and ITPR1, ATXN2 also acts as modulator of RNA splicing and neural excitability (Elden et al., 2010; Liu et al., 2009).

In contrast to the atrophic phenotype in SCA2 patients, loss of ATXN2 in mouse triggers obesity, dyslipidemia, insulin resistance and hepatic accumulation of lipid droplets and glycogen (Lastres-Becker et al., 2008a). *ATXN2* locus polymorphisms in humans were also found associated with obesity, hypertension, diabetes mellitus type 1 and cardiac infarction (Auburger et al., 2014). Strong effects of ATXN2 orthologues on mitochondrial precursor proteins and metabolic enzymes were documented in numerous studies and organisms, further strengthening the modulatory effect of ATXN2 on nutrient metabolism and cellular energetics throughout evolution (Meierhofer, 2016; Seidel et al., 2017; Sen et al., 2016; Sen et al., 2017; Wang and Chen, 2015). Intriguingly, ATXN2 deficiency not only rescues the lethality of yeast PABP deletion (Mangus et al., 1998), but also shows therapeutic promise in flies and mice by mitigating the neurodegenerative process of spinocerebellar ataxias and ALS models (Al-Ramahi et al., 2007; Becker, 2017; Elden et al., 2010; Scoles, 2017).

Currently, there is no curative treatment for SCA2 (Freund et al., 2007). Although several *in vivo* and *in vitro* models for SCA2 were developed, an authentic mouse model mimicking all aspects of the disease was still lacking. Previous animal models largely focused on the overexpression of expanded ATXN2 in Purkinje neurons, so they are unsuitable to study extra-cerebellar deficits or the contribution of other cell types in the central nervous system. Analysis of these mouse mutants showed that ATXN2 protein aggregates accumulate in cytosol rather than the nucleus (Huynh et al., 2000). Purkinje cell-specific Q58- and Q127-ATXN2 expansions alter neuronal excitability (Dell'Orco et al., 2017; Hansen et al., 2013; Liu et al., 2009; Pflieger et al., 2017). Another model with the overexpression of a human Q72-ATXN2 BAC clone containing the physiological promoter and the intact exon-intron structure showed dysregulation of the G-protein signaling factor RGS8 in cerebellum (Dansithong et al., 2015). We recently published the first knock-in (KIN) mouse where normally expressed CAG42-expansion triggers ATXN2 to sequestrate PABP into insolubility in vulnerable brain regions (Damrath et al., 2012). Induction of the ubiquitination enzyme FBXW8 was observed as an effort to degrade Q42-expanded ATXN2 (Halbach et al., 2015). In addition, partial loss-of-function effects were observed to dysregulate calcium homeostasis factors similarly as in *Atxn2*-KO mouse (Halbach, 2017). Unfortunately, the neurological phenotypes appear only after two years in *Atxn2*-CAG42-KIN mice due to slow progression of the disease, making them unsuitable for studying advanced stages of SCA2 within the lifespan of a mouse.

Here, we present a new mouse model of ATXN2 pathology, named *Atxn2*-CAG100-KIN, created by the knock-in of 100 CAG trinucleotide repeat units into the murine *Atxn2* gene with intact murine promoter and exon-intron structure in order to preserve its native expression regulation. Extensive analyses on genetic instability, histology, behavior and in vivo measurements correlate with all aspects of the disease signature observed in patients; they also support the authenticity and value of this model in understanding the molecular mechanisms and in monitoring the disease progression *in vivo* via magnetic resonance spectroscopy. Our initial investigation into the molecular pathogenesis in mouse points to a progressive dysregulation of NAA synthesis in cerebellum, with a strong deficiency of NAA production enzyme *Nat8l*,

which starts from pre-symptomatic stages. Further mechanistic studies proved the direct effect of expanded ATXN2 on diminished *Nat8l* transcript levels also in adipogenic cells. This effect was replicated also in blood of *Atxn2*-CAG100-KIN mice and SCA2 patients, so human *NAT8L* levels show promise as peripheral biomarker.

In this initial study, we have focused on the neuronal aspects of pathology, trying to identify the earliest events that may play an important role in the manifestation and progression of the disease. However, this new model of ATXN2 pathology also allows understanding the involvement of non-neuronal cells in the nervous system, e.g. in view of the role of NAA as a neuron-generated metabolite that is needed for myelination. Our new model also permits the analysis of affected peripheral tissues that have been ignored so far, hopefully leading to the identification of prognostic biomarkers and novel therapies effective at the organism level.

2. Results

2.1. Generation of the Atxn2-CAG100 knock in mouse line and genetic instability

In order to study the progression of neurodegeneration in an authentic rodent model for SCA2, we created the novel *Atxn2*-CAG100 knock-in (KIN) mouse line. For this purpose, a $(CAG)_{100}$ repeat with neighboring sequences was synthesized and inserted into the murine *Atxn2* exon 1 at position Q156 with flanking loxP sites, employing the homologous recombination strategy shown in Fig. 1A and using previously described targeting vectors (Damrath et al., 2012; Lastres-Becker et al., 2008a). Embryonal stem (ES) cell lines with successful knock-in underwent Flp-mediated excision of the neomycin resistance cassette, and verification of the expansion length in heterozygous (CAG1/100) or homozygous (CAG100/100) animals was performed by PCR with Neo-flanking or repeat-flanking primers (Fig. 1B, C, Supplementary Table S1) and Sanger sequencing, resulting in a single homozygous *Atxn2*-CAG100-KIN mouse line.

Genotyping with repeat-flanking primers and with DNA-fragment-length-analysis on polyacrylamide gels initially suggested stability of the expansion size, as previously observed in the *Atxn2*-CAG42-KIN mice (Damrath et al., 2012). In patients, repeat expansions often increase over generations and show a mosaic pattern in the somatic cells (Cancel et al., 1997). To our knowledge, this instability and mosaicism has not been observed in previously generated mouse models of SCA2, while it is a known feature of mice with polyglutamine expansion that model Huntington's disease (Mangiarini et al., 1997). Although genotyping had initially suggested repeat stability in our *Atxn2*-CAG100-KIN mice, periodic testing in successive generations of this colony revealed the occurrence of further expansions and somatic mosaicism (Fig. 1D). The first three panels in Fig. 1D show 3 heterozygous animals from different generations over a period of 4 years, and reveal an increase of the repeat length in time. The calculated PCR product length for the WT allele is 90 bp, whereas the CAG100 allele generates a product of 387 bp. The first mouse has an average expanded allele size of 396.81 bp, with mosaicism ranging from 380 bp to 420 bp. The second mouse shows an exceptional mosaicism range from 405 bp to 476 bp, representing a CAG tract of 128 repeats. The third mouse shows less somatic mosaicism and the average expanded allele length is 470 bp. The bottom panel shows a homozygous KIN animal with no visible WT allele signal at 90 bp, but two expanded alleles with average peaks at 416.65 bp and 475.64 bp. Overall, these findings closely mirror the repeat instability observed in SCA2 patients. To preserve the initial expansion size of the *Atxn2*-CAG100-KIN mouse line, sperm cryopreservation from early generations was carried out. While we keep referring to the animals as *Atxn2*-CAG100-KIN, the CAG-repeat of the animals used was varying within the range shown in Fig. 1D.

2.2. Offspring contains fewer female mutants than expected

It has been shown previously that in the absence of ATXN2, mouse breeding produces less homozygous mutant and less female pups than expected (Kiehl et al., 2006; Lastres-Becker et al., 2008a). Also in invertebrates, gender-related reproductive anomalies have been reported, including female sterility in *D. melanogaster* with ATXN2 mutations and abnormal masculinization of the germline in *C. elegans* with ATX-2 deficiency (Ciosk et al., 2004; Satterfield et al., 2002). For these reasons, gender and genotypes were documented among offspring of 25 CAG1/100 breeder pairs. The litters contained significantly less homozygous mutants than expected (24% less CAG100/100 than WT pups; $p = .009$; χ^2 test with $\chi^2 = 9.384$ and df = 2) and less females than expected (12% reduction; $p = .098$; χ^2 test with $\chi^2 = 2.731$ and df = 2) (Supplementary Table S2). All data suggest that altered ATXN2 functions may impair embryonal development, with some gender-dependence. Thus, the findings constitute evidence for a partial loss-of-function of CAG100 allele in peripheral tissues, and for the high conservation of ATXN2 function during phylogenesis.

2.3. Initial weight excess reverts over time

Phenotypic and behavioral features of heterozygous and homozygous KIN animals were monitored until the end of lifespan. *Atxn2*-CAG100-KIN mice showed progressive motor deficits with hind limb clasping, reduced strength and ataxia (Supplementary Video S1). Homozygous *Atxn2*-CAG100-KIN animals displayed severe motor deficits around 14 months, which prompted the veterinarians to sacrifice the animals to prevent suffering. Therefore, the maximum lifespan is considered to be 14 months for homozygous animals. Even before the terminal stage of disease, homozygous *Atxn2*-CAG100-KIN animals showed an increased rate of death without known reasons ($p < .001$; $\chi^2 = 65.366$; df = 2; Kaplan-Meier survival analysis with Tarone-Ware test; Fig. 2A).

Although all mutants eventually developed a loss of weight compared to WT littermates, female homozygous *Atxn2*-CAG100-KIN animals initially displayed excess weight gain between 5 and 20 weeks. As the disease progressed, they not only lost this extra weight, but went further on towards an atrophic state. Female heterozygotes also showed reduced body mass in later disease stages, but without the initial weight gain ($p < .001$; $F = 70.524$ with 23 degrees of freedom; two-way ANOVA; Fig. 2B). In male mutants, we did not observe the initial weight excess, but they also showed a progressive weight loss relative to WT animals ($p < .001$; $F = 121.651$ with 23 degrees of freedom; two-way ANOVA; Fig. 2C). In male mutants, weight loss became significant already at the age of 10 weeks in heterozygous mice and at 20 weeks in homozygous mice. Even though the homozygous males started to lose weight later than their heterozygous littermates, their weight reduction developed faster and stronger (Fig. 2C). The temporal dynamics of body weight across lifespan might reflect an initial partial loss-of-function phenotype due to the reduced levels and insolubility of expanded ATXN2, followed by the progressive accumulation in cytosolic aggregates with consequent gain-of-function phenotypes.

Eventually, all the mutant mice displayed weight loss, but the time course depended on the dosage of expanded ATXN2 allele and on gender. This is in good agreement with previous reports stating that homozygous SCA2 patients also have earlier disease onset and a particularly severe disease course (Hoche et al., 2011; Ragothaman et al., 2004). Therefore, in order to investigate the maximal pathology and to avoid gender-specific bias, we focused on homozygous animals without gender separation in further neuropathological and expression analyses.

2.4. Initial hyperactivity disappears with ageing; progressive motor deficits are compatible with spinocerebellar ataxia

To determine whether the *Atxn2*-CAG100-KIN mice displayed motor deficits compatible with symptoms observed in SCA2 patients, we

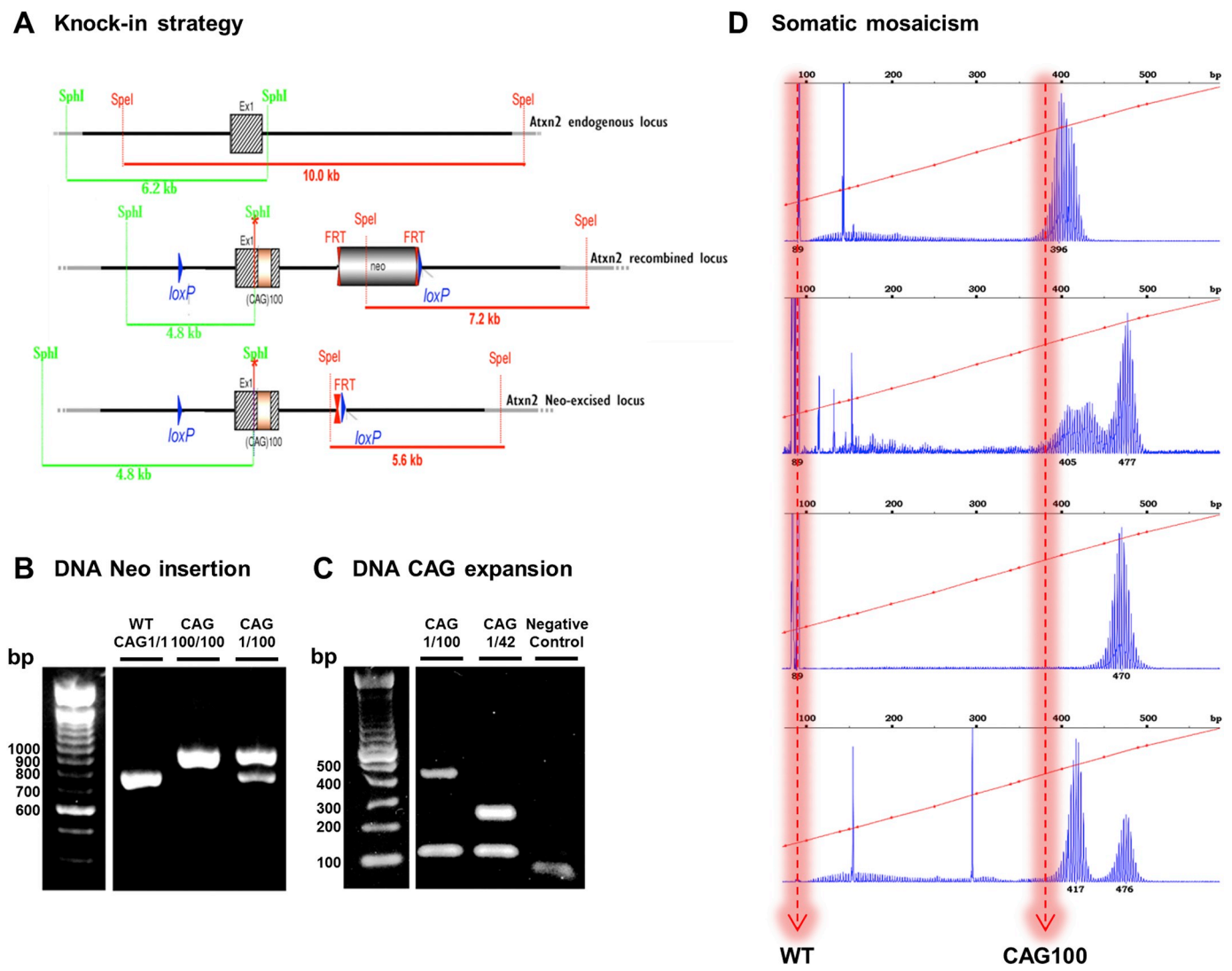

Fig. 1. Generation of *Atxn2*-CAG100 expansion and CAG repeat instability over generations. (A) Schematic diagram of the knock in strategy at exon 1 (Ex1) of the murine *Atxn2* gene on chromosome 5. Names of the restriction enzymes (*Sph*I, *Spe*I), expected restriction fragment sizes in kilobases (kB) and position of loxP/FRT target sites of recombinases are marked, which were relevant in the homologous recombination screening and subsequent excision of the Neo-selection cassette. (B) Agarose gel electrophoresis results of genotyping PCR with primers flanking the Neo-excised locus (size of PCR product for CAG1 = 793 bp, CAG100 = 948 bp) and (C) primers flanking the CAG site (size of PCR product for CAG1 = 90 bp, CAG100 = 387 bp, CAG42 = 213 bp). As negative control, water instead of template DNA produced a lower-size band that represents PCR primers. (D) Fragment length analysis of the CAG repeat in three heterozygous (top three panels) and one homozygous knock-in (lower panel) mice. Predicted PCR fragment length of wild type allele is 90 bp, predicted PCR fragment length of CAG100 allele is 387 bp. While the WT allele gives a sharp peak at 90 bp level, all expanded alleles show a hedgehog-like pattern that reflects somatic mosaicism.

conducted a series of behavioral tests in older mice. Paw print analyses were performed to assess free movements in a narrow dark tunnel where the mice walk from one end to the other. Paw prints of *Atxn2*-CAG100-KIN mice at 12 months showed irregular steps and uncoordinated movement (Fig. 2D). To evaluate the particularly vulnerable motor neurons, grip strength analyses were done with *Atxn2*-CAG100-KIN animals from the age of 3 months onward, which revealed a significant decrease in the maximal forelimb efforts over time ($p < .001$; $F = 10.219$ with 7 degrees of freedom; ANOVA). Around the age of 11 months, the forelimb grip strength of *Atxn2*-CAG100-KIN mice became significantly less, while it remained intact in WT littermates ($p < .001$; $F = 9.964$ with 15 degrees of freedom; two-way ANOVA; Fig. 2E). Tests of the motor coordination ability and tenacity to stay on a rotating rod upon slow acceleration showed a significant and stable deficit in *Atxn2*-CAG100-KIN mice from the age of 20 weeks to 12 months, which progressed rapidly at 14 months. Heterozygous *Atxn2*-CAG100-KIN animals appeared normal on the rotarod ($p < .001$; $F = 13.871$ with 14 degrees of freedom; two-way ANOVA with Tukey's post-hoc tests: WT vs. CAG100/100: $p < .001$; WT vs. CAG1/100: $p = .978$; Fig. 2F). Open field tests were conducted to assess spontaneous activity and various motor impairments. Homozygous *Atxn2*-CAG100-KIN animals showed an initial hyperactivity period around the age of 10 weeks in terms of movement time, total distance travelled and horizontal movements (Fig. 2G), as previously described also in *Atxn2*-KO mice (Lastres-Becker et al., 2008a). However, reductions were observed in *Atxn2*-CAG100-KIN animals for all vertical behavior parameters starting from early ages, and worsening progressively (Fig. 2G). These severe deficits in vertical movement indicate problems in balancing upright for explorative or food-seeking purposes, and mirror the gait ataxia in SCA2 patients.

2.5. Deleterious effects of the CAG100 expansion on the transcription and translation of Atxn2

The expanded size of *Atxn2* mRNA was confirmed by saturation reverse transcriptase (RT)-PCR in cerebellum of heterozygous (CAG1/

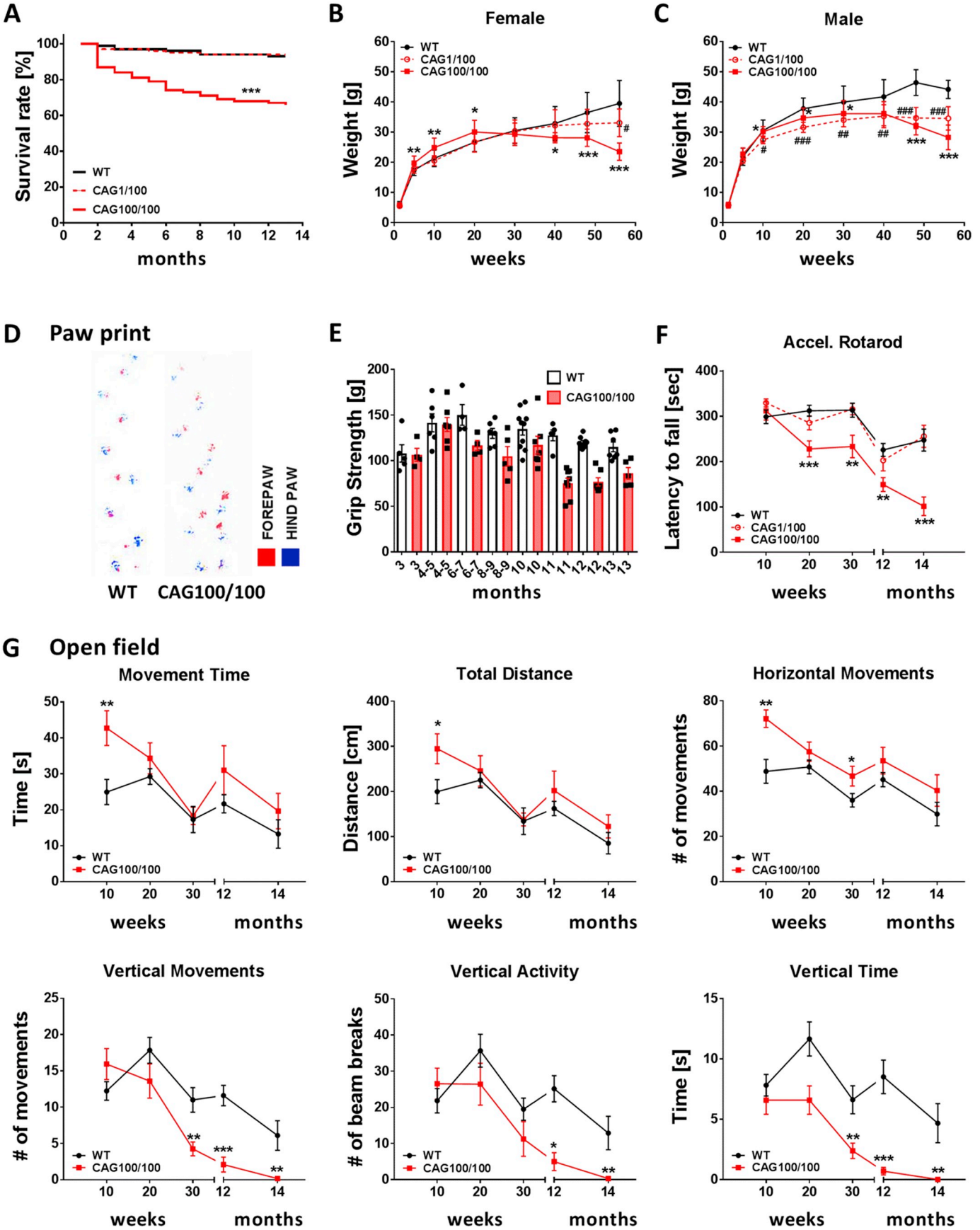

(caption on next page)

Fig. 2. Lifespan, weight and motor phenotypes of *Atxn2*-CAG100-KIN mice across ages. (A) The reduction of the ageing cohort through animals found dead at different ages is shown across the lifespan, before all animals were sacrificed for ethical reasons (100% corresponds to 106 CAG100/100, 235 CAG1/100 and 167 WT animals born initially). (B) Body weight of female and (C) male animals was studied in groups of 4–19 mice per genotype and age. Data is represented as means ± s.d. (D) Paw prints were recorded in 13 WT and 9 CAG100/100 animals at the age of 12 months. (E) Grip strength was assessed in 4–10 animals at the ages indicated. (F) The latency to fall from a rotarod slowly accelerating from 4 to 40 rpm reflected a very early motor deficit among CAG100/100 homozygotes (n = 22 animals per genotype for younger age groups, n = 8 animals for old ages). (G) Open field analyses of the spontaneous movement activity of mice during a 5 min observation period in an odor-neutral arena recorded in automated manner via infra-red beam breaks for various parameters of locomotion (n = 8–23 animals per age and genotype). (For interpretation of the references to colour in this figure legend, the reader is referred to the web version of this article.)

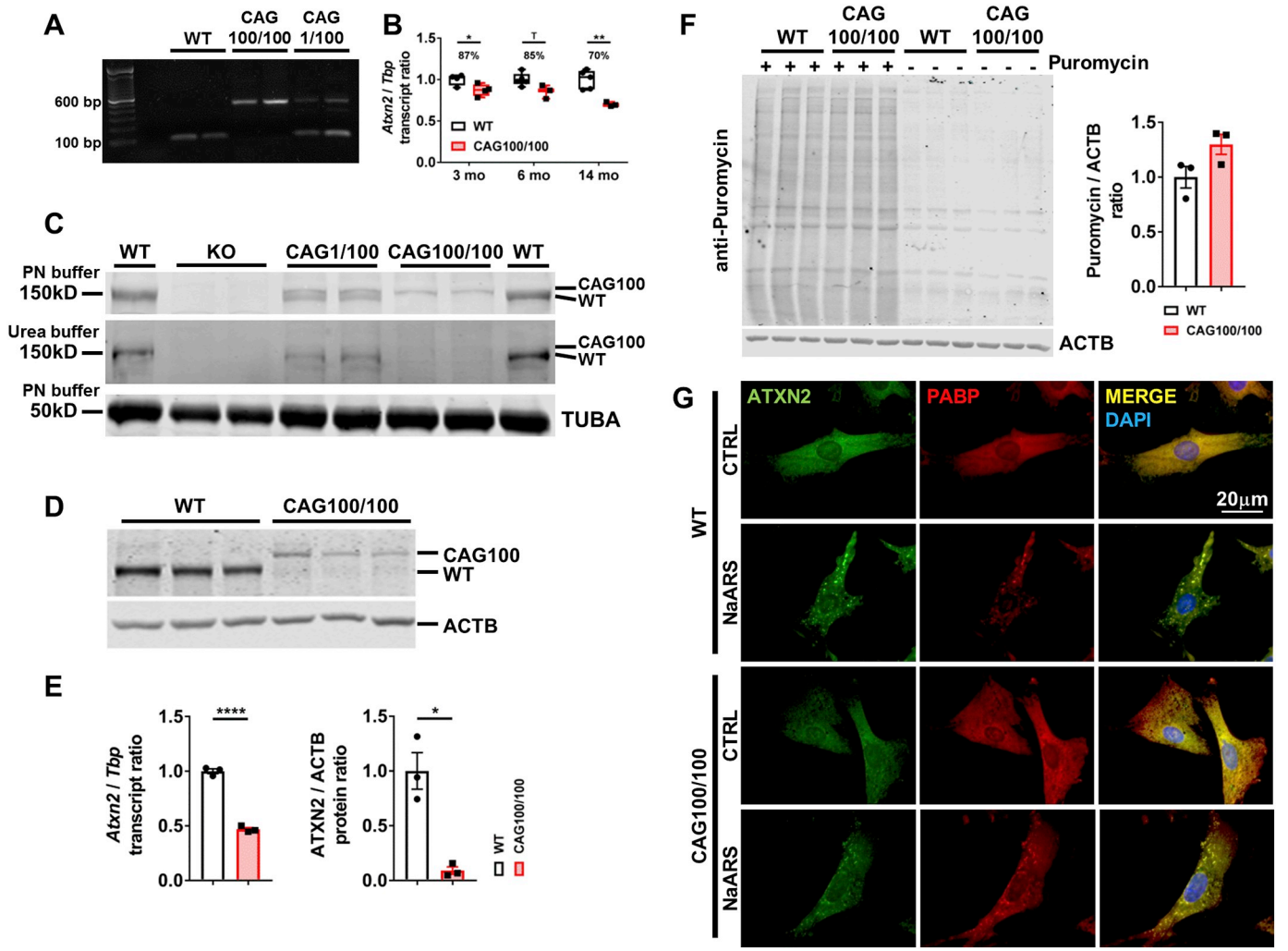

Fig. 3. CAG100 allele shows major protein insolubility, despite mild transcript changes in cerebellum. (A) Analysis of cerebellar cDNA by RT-PCR with primers flanking the CAG site demonstrated the presence of expansion in *Atxn2* mRNA from heterozygous (CAG1/100) and homozygous (CAG100/100) knock-in animals. (B) Expression analysis of *Atxn2* transcript in CAG100/100 cerebellar cDNA showed mild reduction that progressed with age. Statistical analyses were done by unpaired *t*-test with Welch's correction. Box-whiskers plot shows individual values with median and min to max confidence interval. (C) Detection of ATXN2 protein in WT, *Atxn2*-knock out (KO), heterozygous and homozygous *Atxn2*-CAG100-KIN mice cerebellum protein lysates isolated with low-detergent (PN) and high-detergent (Urea) buffers at the age of 14 months. The CAG100 allele in both heterozygous and homozygous knock in animals shows reduced protein abundance compared to the wild type CAG1 allele in PN buffer lysates. A fraction of the WT allele is visible in the Urea buffer lysate of WT and CAG1/100 animals. A faint signal is detected for the expanded CAG100 allele in heterozygous animals, no signal is detected in homozygous animals. (D) ATXN2 immunoblot of 3 different primary murine embryonal fibroblast (MEF) clones from WT and *Atxn2*-CAG100-KIN animals show significantly reduced abundance of CAG100 allele. (E) *Atxn2* mRNA levels measured in 3 different *Atxn2*-CAG100-KIN MEF clones showed a reduction to 47% (p < .0001) compared to their WT pairs. Quantification of ATXN2 protein levels (blot shown in panel A) showed a reduction to 9% (p = .0283) in RIPA lysate. No protein was detected in high-detergent containing SDS lysate (data not shown). Statistical analyses were done by Ratio paired t-test. Bar graphs show individual values together with mean ± s.e.m. (F) Puromycin incorporation analysis in 3 different WT and *Atxn2*-CAG100-KIN MEF clones showed no significant difference in global translation rate. Statistical analysis was done by Ratio paired t-test. Bar graph shows individual values together with mean ± s.e.m. (G) Immunocytochemical detection of ATXN2 localization in WT and *Atxn2*-CAG100-KIN MEFs under normal (CTRL) and sodium arsenite (NaARS, 0.5 mM, 45 min) induced oxidative stress conditions. Both WT and expanded ATXN2 localize to stress granules under stress. ACTB: beta-actin, TUBA: alpha-tubulin.

100) and homozygous (CAG100/100) knock-in mice (Fig. 3A). The expression level of the expanded *Atxn2* mRNA was measured at 3 months, 6 months and 14 months, which are the important time points in the lifespan of *Atxn2*-CAG100-KIN colony according to phenotypic and behavioral assessments presented in Fig. 2. Expanded *Atxn2* mRNA showed a significant, yet small reduction to 87%

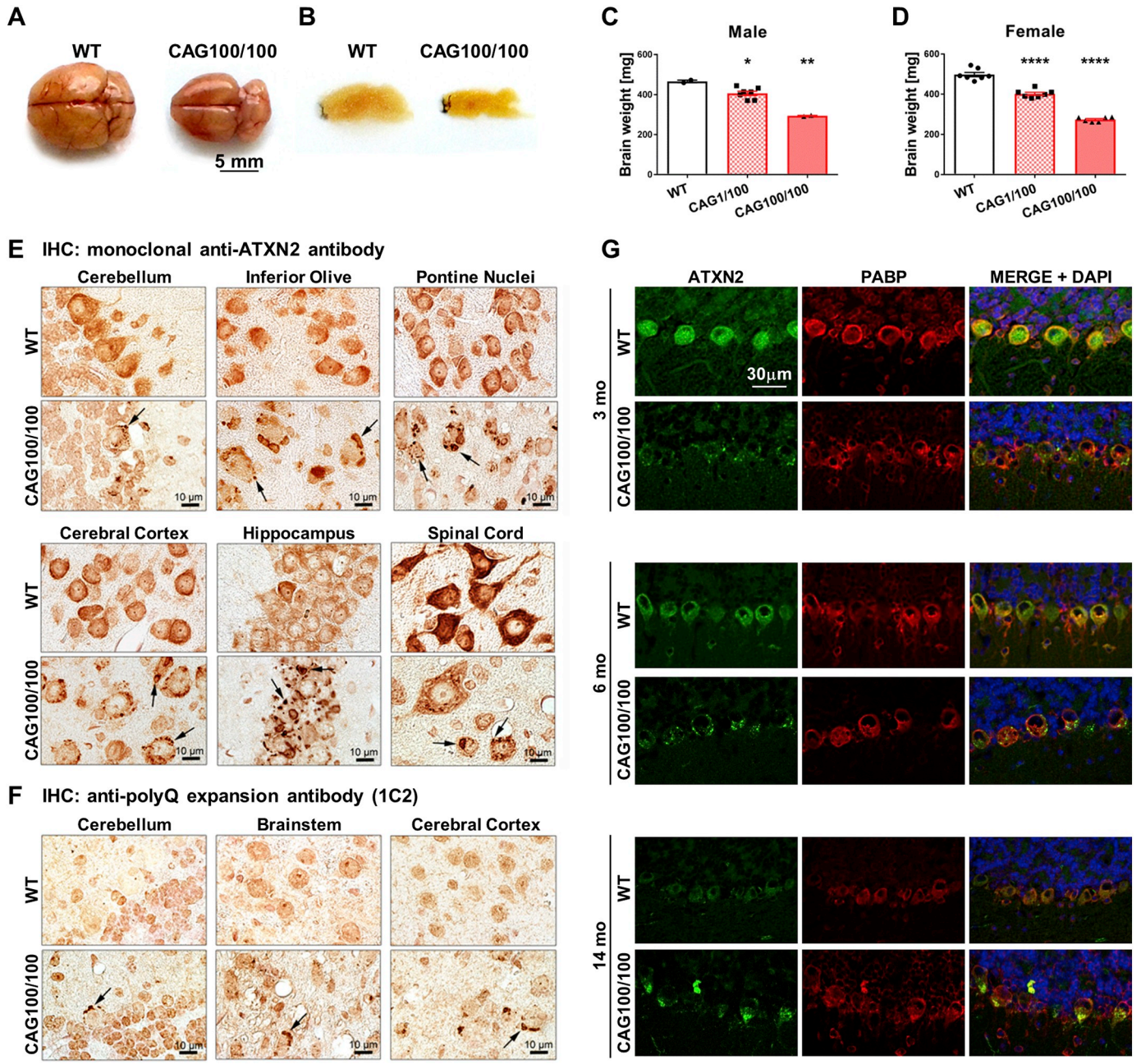

Fig. 4. Brain pathology of *Atxn2*-CAG100-KIN mice at the age of 14 months. (A) Representative brain photos are shown after sacrifice (seen from above) and (B) after dehydration and embedding in paraffin (as sagittal section). Statistical evaluation of brain weight for WT, heterozygous (CAG1/100), and homozygous (CAG100/100) animals was assessed separately for male (C) and female (D) animals (for males, reduction to 0.81% vs. 0.55%, $p = .03$ vs. 0.001; for females, reduction to 0.87% vs. 0.63%, $p < .00001$ vs. $< .00001$; tested by ANOVA with multiple testing correction after Bonferroni). Bar graphs show individual values together with mean ± s.e.m. (E) Immunohistochemical (IHC) visualization of puncta or large aggregates across various brain regions using paraffin-embedded sections stained with ATXN2 and (F) monoclonal polyQ expansion antibody 1C2 using DAB detection. (G) Immunofluorescent staining of ATXN2 and PABP in cerebellum of WT and *Atxn2*-CAG100-KIN mice across ages.

($p = .0418$) at 3 months, decreased to 85% ($p = .0669$) at 6 months, and decreased further to 70% ($p = .0029$) at 14 months, which is the terminal stage of the disease (Fig. 3B).

Next, we studied the abundance and solubility of the expanded ATXN2 protein in cerebellum of heterozygous (CAG1/100) and homozygous (CAG100/100) knock-in animals at 14 months (Fig. 3C). Expanded ATXN2-CAG100 protein was visible in the soluble fraction obtained by low-detergent PN buffer in both heterozygous and homozygous knock-in animals. However, the ATXN2-CAG100 allele abundance in both genotypes was reduced compared to the WT allele. The insoluble or membrane-bound protein fraction obtained by high-detergent Urea buffer showed a portion of the normal ATXN2 allele in WT and heterozygous (CAG1/100) animals. Although a small fraction of expanded CAG100 allele was visible in the Urea fraction in heterozygous animals, no ATXN2-CAG100 signal was detected in the Urea fraction of homozygous animals (Fig. 3C). This loss of the urea-soluble ATXN2-CAG100 is probably due to the ongoing aggregation process. It is well established that expanded ATXN2 protein tends to form intracellular aggregates that sequestrate known interactor proteins such as Poly(A)-Binding Protein (PABP), as shown in previously generated mouse models and SCA2 patients (Damrath et al., 2012). In the previously generated *Atxn2*-CAG42-KIN mice, which showed only mild

neurological signs at the end of normal mouse lifespan, the expanded ATXN2 protein in the aggregates could be solubilized and observed in immunoblots with both RIPA and SDS/Urea buffers (Damrath et al., 2012), whereas the ATXN2-CAG100 could not be solubilized by Urea. This ATXN2-CAG100 deficiency (Fig. 3C) might be partially explained also by inefficient translation of the expanded *Atxn2* mRNA, given that this expansion in the DNA also seems to decrease the *Atxn2* transcript production or stability (Fig. 3B).

In order to study the protein dynamics of ATXN2-CAG100, different clones of primary murine embryonal fibroblast (MEF) lines were generated from WT and homozygous *Atxn2*-CAG100-KIN animals. Under normal culture conditions, the expanded ATXN2 protein was detectable only in RIPA lysate of both WT and *Atxn2*-CAG100-KIN cells (Fig. 3D). No ATXN2 protein was detected in SDS lysate (data not shown). Quantification of the expanded *Atxn2* transcript in these cells revealed a reduction to 47% (Fig. 3E, $p \leq .0001$), and quantification of the protein signal presented in Fig. 3D revealed a drastic reduction to 9% ($p = .0283$). To rule out the possibility that *Atxn2*-CAG100-KIN affect PABP-dependent mRNA translation at the global level, puromycin-incorporation assays were carried out with three different MEF clones. They observed no significant difference in overall translation rate between normal and mutant cells (KIN 130%, $p = .2280$) (Fig. 3F). Immunocytochemical analysis of MEF under normal culture conditions showed a diffuse cytosolic distribution of ATXN2 in both WT and *Atxn2*-CAG100-KIN cells (Fig. 3G). PABP also showed diffuse cytosolic localization as expected. As established for WT cells, also in *Atxn2*-CAG100-KIN cells both ATXN2 and PABP localized to cytoplasmic ribonucleoprotein particles known as stress granules (SG), when oxidative stress occurred upon sodium-arsenite (NaARS) treatment. Thus, in peripheral cells the expanded ATXN2 protein was severely reduced in abundance, but had the correct subcellular localization and its stress-response capabilities remained intact.

Overall, these observations indicate that the CAG100 expansion reduces the total protein levels of soluble ATXN2. Thus, loss-of-function effects will be prominent in peripheral cells, where the aggregation of the expanded disease protein does not occur, which is excitation-induced and restricted to postmitotic cells such as neurons (Koch et al., 2011).

2.6. Progressive brain atrophy and neuronal aggregation throughout the central nervous system

At the terminal stage of the disease, analysis of the *Atxn2*-CAG100-KIN brain revealed atrophy and weight loss for both sexes in homozygous mice, and to a lesser extent also in heterozygous mice despite the lack of neurological disease signs at that age (Fig. 4A–D). Immunohistochemical analysis of ATXN2 protein with a monoclonal antibody in WT and *Atxn2*-CAG100-KIN brains revealed high signals in many neuron populations, particularly in specific brainstem nuclei (inferior olive and pons), cerebellum, ventral forebrain areas, cerebral cortex and hippocampus, showing good agreement with publically available in-situ hybridization data of wild type mice at the Allen Brain Atlas (Supplementary Fig. S1). Upon further examination by light microscopy, cytosolic aggregates of ATXN2-CAG100 were observed in the typical regions affected by neurodegeneration in SCA2 (Estrada et al., 1999; Giuffrida et al., 1999), such as cerebellar Purkinje neurons, inferior olivary neurons and pontine nuclei neurons (Fig. 4E upper rows). Aggregates were also detectable in cerebral cortical and hippocampal neurons and in spinal cord motor neurons, where they were particularly large (Fig. 4E lower rows). In all these regions, the cytosolic aggregates were confirmed to contain expanded ATXN2 protein upon immunostaining with the monoclonal anti-polyQ antibody 1C2 (Fig. 4F). Further investigation of the cerebellar Purkinje neurons via electron microscopy also confirmed the presence of cytosolic protein aggregates (black arrowheads in Supplementary. Fig. S2). As cerebellar dysfunction and neuropathology are considered the most prominent and common aspects of dominant ataxias, we focused on cerebellar ATXN2 pathology and its progression throughout lifespan in *Atxn2*-CAG100-KIN mice. Immunofluorescent detection of ATXN2, together with its known interactor PABP, was performed in 3-, 6- and 14-month-old mice cerebella (Fig. 4G). ATXN2 was found highly expressed in Purkinje cells, and showed a diffuse distribution in WT samples across all ages. ATXN2-CAG100, on the other hand, was found accumulated in numerous smaller aggregates starting from the pre-symptomatic age of 3 months. Insolubility of the mutant ATXN2 protein and size of the aggregates increased progressively with age; showing multiple larger puncta at 6 months and a very large unified aggregate towards the axon hillock at 14 months. PABP signal in WT samples was also found highly expressed in Purkinje cell soma throughout lifespan. Although the small aggregates in *Atxn2*-CAG100-KIN cerebellum at 3 months did not seem to sequester PABP into insolubility, larger ATXN2-CAG100 aggregates starting from 6 months also showed PABP immunoreactivity, which was severely worsened at 14 months (Fig. 4G).

Double immunofluorescence was able to show the co-localization of ATXN2-positive cytosolic aggregates with ubiquitin signals (Supplementary Fig. S3A) and p62 signals (Supplementary Fig. S3B) in cerebellum, brainstem and spinal cord, suggesting that they undergo the classical elimination via autophago-lysosomal pathways (Lee et al., 2015). Again, particularly large protein aggregates could be observed in spinal cord motor neurons (Supplementary Fig. S3, lowest row), in good agreement with the preferential vulnerability of motor neurons in pre-symptomatic stages of human SCA2 (Velazquez-Perez et al., 2014). Thus, the neuropathological pattern in *Atxn2*-CAG100-KIN mouse closely mirrors the selective vulnerability of specific neuron populations known from human SCA2.

2.7. Significant reductions of N-acetylaspartate and glutamate levels in Atxn2-CAG100-KIN cerebellum in vivo

After establishing that *Atxn2*-CAG100-KIN mice bear the genetic, behavioral and neuropathological hallmarks of SCA2, we used magnetic resonance imaging to study the mice *in vivo* and employed spectroscopy to assess whether molecular changes occur similar to patients. Data of the right cerebral hemisphere and middle part of the cerebellum were collected from age- and sex- matched WT and *Atxn2*-CAG100-KIN animals between the ages 12 and 14 months. Fig. 5A shows representative images for voxel positioning and the spectra obtained. Quantification of the main peaks showed a general decrease in total *N*-acetylaspartate (tNAA = NAA and NAAG), glutamate (Glu) and choline (Cho) levels when normalized to myoinositol (MI) in both cerebellum and cerebrum, while creatine (Cre) remained unchanged (Fig. 5A). Pairwise statistical analyses revealed that only tNAA (57%, $p = .0241$) and Glu (77%, $p = .0192$) reductions in cerebellum reached significance, whereas other metabolites suffered from high variation among controls. A decrease in NAA levels has been observed before in the context of many neurodegenerative disorders, and is considered to be a biomarker of neuronal dysfunction or death (Ariyannur et al., 2010). Large cohort studies with autosomal dominant cerebellar ataxia and multiple system atrophy (MSA) patients demonstrated a reduction in tNAA levels in most of subtypes of spinocerebellar ataxia, however tNAA deficit has the highest correlation with SCA2 pathology and progression among all disease types investigated (Cahill Jr. and Veech, 2003; Wang et al., 2012).

Overall, the spectroscopic and histological analyses of *Atxn2*-CAG100-KIN mouse brain showing the spatio-temporal neuropathology pattern known from SCA2 patients, together with the previously shown features of somatic mosaicism, fertility changes and progressive motor dysfunction, collectively prove the authenticity and value of this newly generated mouse model of Ataxin-2 pathology.

2.8. Important factors of NAA metabolism are altered in Atxn2-CAG100-KIN mouse cerebellum

Taking advantage of our new SCA2 mouse model to study earliest

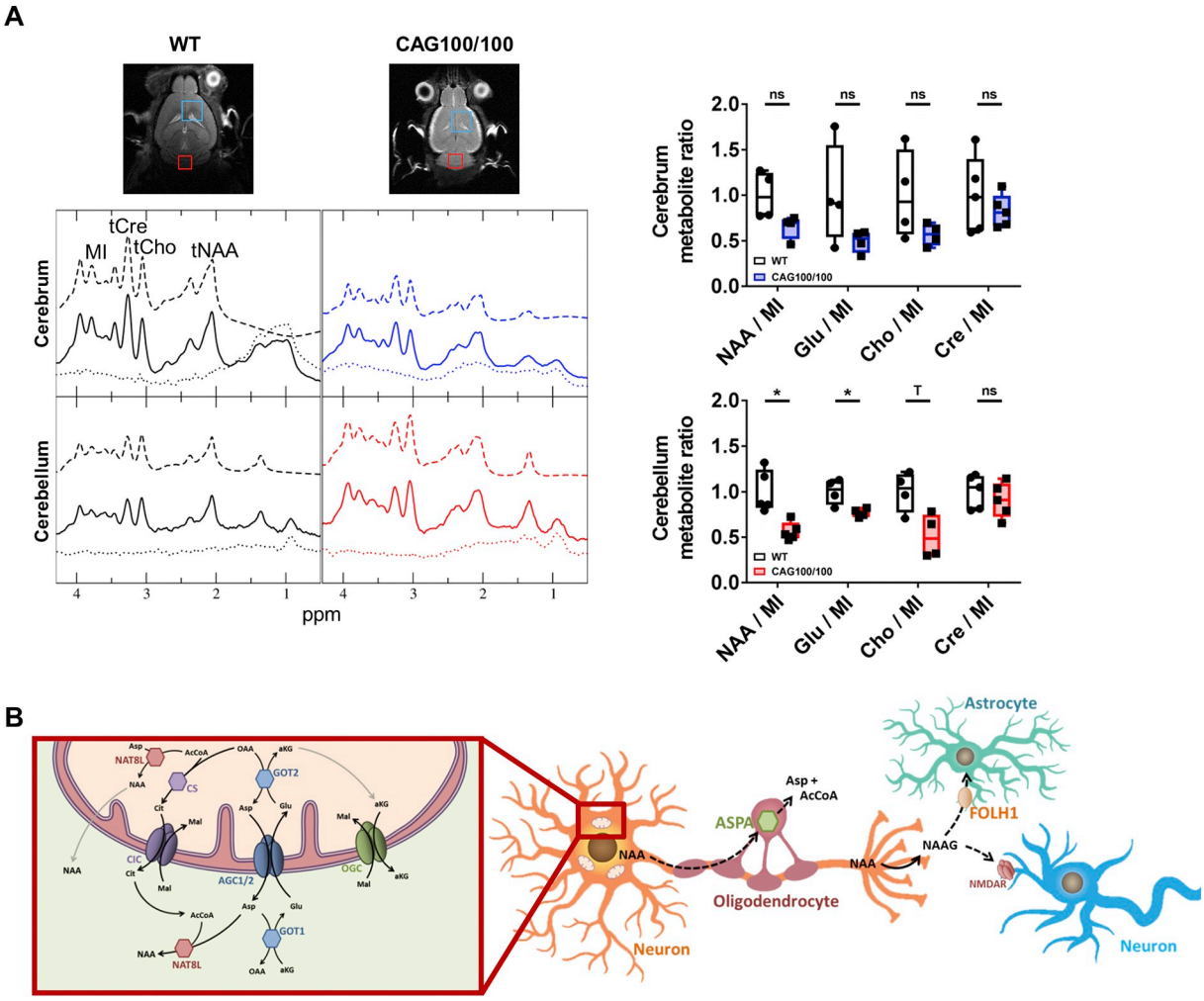

Fig. 5. Altered *N*-acetylaspartate (NAA) and glutamate (Glu) levels in *Atxn2*-CAG100-KIN mouse cerebellum. (A) Magnetic resonance spectroscopy of WT and *Atxn2*-CAG100-KIN mice showed significantly reduced NAA and glutamate levels in cerebellum (in red), but not in cerebrum (in blue) when normalized to myoinositol (MI) levels. Representative images show the approximate regions from where the data was acquired in cerebrum (blue boxes) and cerebellum (red boxes). Representative spectrograms are shown for both cerebellar and cerebral measurements in WT and CAG100/100 animals (dashed lines: fitted data, solid lines: original spectrum data, dotted lines: residuum). Statistical analyses were done by Ratio paired t-test. Box-whiskers plot shows individual values with median and min to max confidence interval. Cerebellum: NAA: 57%, $p = .0241$; Glu: 77%, $p = .0192$; Cho: 48%, $p = .0616$; Cre: 90%, $p = .5217$. Cerebrum: NAA: 67%, $p = .1578$; Glu: 54%, $p = .1889$; Cho: 61%, $p = .2392$; Cre: 87%, $p = .6136$. (B) Schematic illustration of NAA metabolism within neurons and among different cell types in the nervous system. AcCoA: acetyl-coA, AGC1/2: Mitochondrial Aspartate Glutamate Carrier 1/2, aKG: alpha-ketoglutarate, Asp: aspartate, ASPA: Aspartoacetylase, CIC: Citrate Transport Protein, Cit: citrate, CS: Citrate Synthase, FOLH1: Folate Hydrolase 1, Glu: glutamate, GOT1: Glutamic-Oxaloacetic Transaminase 1, GOT2: Glutamic-Oxaloacetic Transaminase 2, Mal: malate, NAA: *N*-acetylaspartate, NAAG: *N*-acetylaspartylglutamate, NAT8L: N-Acetyltransferase 8 Like, NMDAR: *N*-methyl-D-aspartate receptor, OAA: oxaloacetate, OGC: Mitochondrial 2-Oxoglutarate/Malate Carrier Protein. (For interpretation of the references to colour in this figure legend, the reader is referred to the web version of this article.)

stages of pathology, we asked what enzymatic changes underlie the altered NAA metabolism, and how early the molecular dysregulations occur. Fig. 5B depicts the major aspects of NAA production, intercellular transport and utilization. NAA is synthesized via N-terminal acetylation of aspartate by the enzyme N-Acetyltransferase-8-Like (NAT8L) in neurons (Ariyannur et al., 2010). Although some studies suggested that NAT8L is localized in the cytoplasmic/ER compartment, increasing numbers of studies provided evidence that NAT8L is a mitochondrial/microsomal protein (Ariyannur et al., 2008; Ariyannur et al., 2010; Kedersha and Anderson, 2007; Lu et al., 2004; Wang et al., 2012). Following its synthesis and export into neuronal cytoplasm, NAA is transported into the oligodendrocytes where it is broken down by the enzyme Aspartoacetylase (ASPA) into aspartate and acetate residues. Acetate is further processed into acetyl-CoA and utilized in the production of fatty acids for myelination (Jaeken et al., 1984). A portion of NAA can be converted into *N*-acetylaspartylglutamate (NAAG) at the axon termini and secreted into synaptic cleft as a modulator of glutamatergic excitation. Excess NAAG in the synapse is taken up by the astrocytes through the transporter protein Folate Hydrolase 1 (FOLH1) to prevent excitotoxicity, converted back into NAA and excreted from the CNS to the blood stream (Besse et al., 2015).

We studied the transcript and protein levels of three enzymes that conduct important steps in NAA turnover; NAT8L, ASPA and FOLH1. In order to delineate the causality chain of expression alterations, we examined these enzymes at pre-symptomatic, early symptomatic and terminal stages of the disease in *Atxn2*-CAG100-KIN mouse cerebellum (Fig. 6A). At the transcript level, *Nat8l* showed a significant reduction in all ages studied; starting with a reduction to 76% ($p = .0080$) at 3 months, progressing to 67% ($p = .0018$) at 6 months and further down to 46% ($p = .0003$) in 14-month-old animals. In comparison, *Aspa* mRNA only showed a significant reduction to 72% ($p = .0425$) at the early symptomatic stage of 6 months, and was progressively diminished to 50% ($p = .0020$) in 14-month-old animals. Transcript levels of the NAAG uptake protein *Folh1* only became significantly

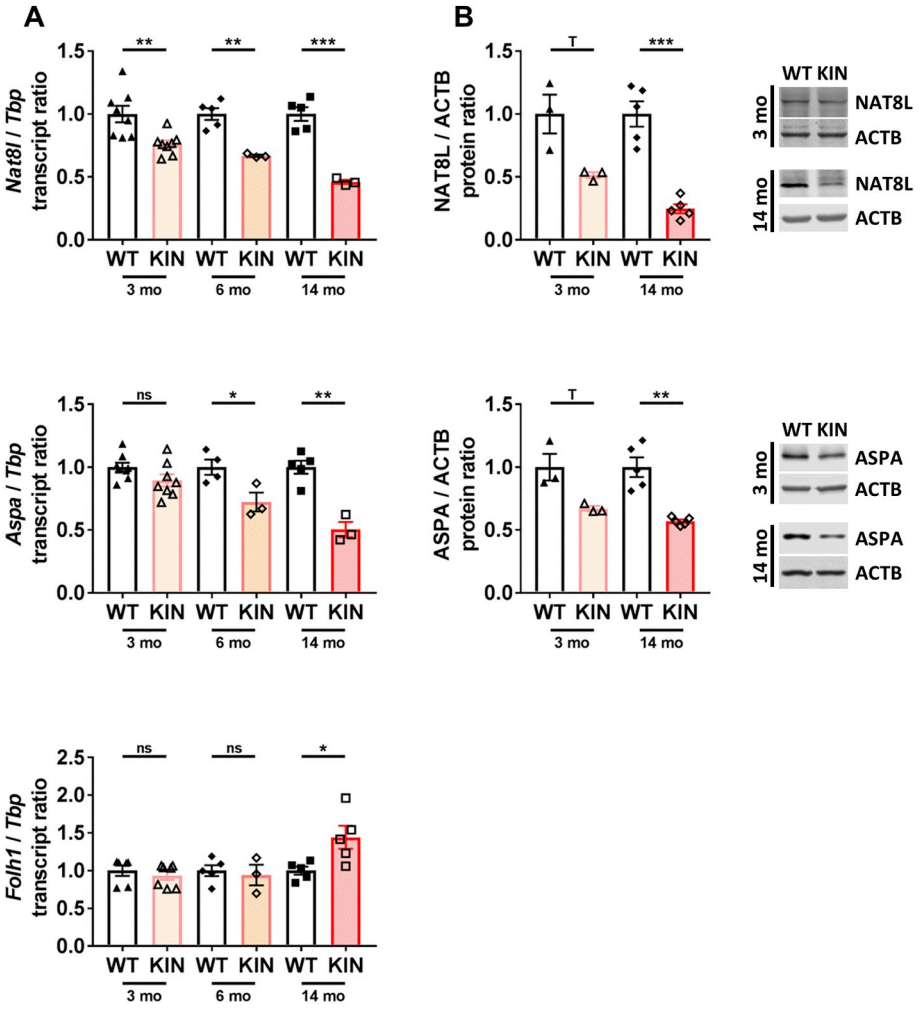

Fig. 6. Transcript and protein levels of NAA metabolism enzymes in cerebellum across ages. (A) Transcript and (B) protein levels of key components in NAA synthesis (NAT8L), NAA breakdown (ASPA) and NAAG transport into astrocytes for excretion (FOLH1) were measured in *Atxn2*-CAG100-KIN mouse cerebellum with WT controls at indicated ages. Statistical analyses were done by unpaired t-test with Welch's correction. Bar graphs show individual values together with mean ± s.e.m. ACTB: beta-actin, mo: months old, T: trend towards significance ($.05 < p < .10$).

affected at the terminal stage of the disease with an increase to 140% ($p = .0425$) at 14 months (Fig. 6A). At the protein level, NAT8L showed a similar expression profile to that of its transcript at respective ages; a decrease to 51% ($p = .0847$) at 3 months and stronger dysregulation down to 25% ($p = .0009$) in 14-month-old animals (Fig. 6B). Protein levels of ASPA at the pre-symptomatic stage of 3 months showed a reduction to 67% ($p = .0838$), and was progressively decreased to 57% ($p = .0047$) at the terminal stage of the disease (Fig. 6B). Protein levels of FOLH1 could not be assessed due to the lack of a reliable antibody for immunoblotting.

All in all, the expression data suggest that the first dysregulation of the NAA metabolism occurs in the synthesis of NAA by NAT8L in neurons starting from pre-symptomatic stage. This is followed by a reduction in oligodendrocytic ASPA levels at early symptomatic stage, which may be an adaptive mechanism to reduced NAA production and supplementation into glia. Finally, the transcript levels of FOLH1 being induced only at the terminal stage of disease indicates that the excitotoxicity burden in the synapses increases during disease progression.

2.9. Dysregulation of NAA production is not due to mislocalization or altered turnover of associated metabolites

After establishing that early in the disease course the generation of NAA is affected, we focused on enzymes that regulate the mitochondrial/cytoplasmic shuttling and availability of the relevant metabolites for this pathway within the neurons. As depicted in Fig. 5B, there are three types of metabolite shuttle proteins for the transport of metabolites across mitochondrial membranes. AGC1 (encoded by *Slc25a12* gene) and AGC2 (*Slc25a13*) are responsible for aspartate-glutamate transport, CIC (*Slc25a1*) is responsible for citrate-malate transport and OGC (*Slc25a11*) is responsible for malate-α-ketoglutarate transport. Inside the mitochondrial matrix, glutamate and oxaloacetate can be metabolized by Glutamic-Oxaloacetic Transaminase 2 (GOT2) into aspartate and α-ketoglutarate. The inverse reaction of aspartate and α-ketoglutarate forming glutamate and oxaloacetate is catalyzed by Glutamic-Oxaloacetic Transaminase 1 (GOT1) in the cytoplasm. Oxaloacetate, together with acetyl-CoA, can also be metabolized to citrate by Citrate Synthase (CS) in mitochondria (Fig. 5B).

Measurement of the metabolite transporters showed only minor downregulations in 14-month-old *Atxn2*-CAG100-KIN mouse cerebellum (Supplementary Fig. 4A); *Slc25a12* (93%, $p = .5114$), *Slc25a13* (84%, $p = .0719$), *Slc25a1* (80%, $p = .0026$) and *Slc25a11* (90%, $p = .0576$). Measurement of enzymes involved in metabolic processes also showed only minor downregulations in 14-month-old *Atxn2*-CAG100-KIN mouse cerebellum (Supplementary Fig. 4A); *Got1* (82%, $p = .0019$), *Got2* (89%, $p = .1022$), *Cs* (81%, $p = .0057$). Among these enzymes, AGC1 and GOT2 were also studied at the protein level in 14-month-old *Atxn2*-CAG100-KIN mouse cerebellum, as they are directly

involved in aspartate metabolism. No significant change was observed for both enzymes in RIPA soluble lysate (Supplementary Fig. 4B; AGC1: 86%, $p = .3352$, GOT2: 120%, $p = .0543$). Since both AGC1 and GOT2 are mitochondrial membrane-bound or -encapsulated proteins, SDS lysates were also tested to eliminate the possibility of mitochondria not being fully solubilized by RIPA buffer. Again, no significant difference were seen in both proteins (Supplementary Fig. 4B; AGC1: 94%, $p = .4093$, GOT2: 76%, $p = .0547$). This set of results suggests that the NAA production deficit is due to altered NAT8L levels in *Atxn2*-CAG100-KIN mouse, but not due to unavailability, mislocalization or deranged metabolism of aspartate or any associated metabolite.

2.10. ATXN2 modulates Nat8l expression in adipogenic fate and peripheral blood

While most studies focus on the role of NAT8L in the central nervous system for NAA production and myelination, this enzyme is also known to be an important regulator of adipogenic fate in the peripheral tissues (Huber et al., 2019; Kedersha and Anderson, 2007; Prokesch et al., 2016). In order to mechanistically show the direct effect of mutant ATXN2 on the transcriptional dysregulation of *Nat8l*, we treated WT and *Atxn2*-CAG100-KIN MEFs with an adipogenic differentiation regimen for 7 days as depicted in Fig. 7A. Expression profiling confirmed the successful induction of adipogenesis, as indicated by the massive upregulation of *Adipoq* (WT 100% to 3000%; KIN 180% to 3400%) as a marker of adipogenesis (Fig. 7B). Under the same conditions, *Atxn2* transcript showed a significant 1.4-fold induction in both WT and *Atxn2*-CAG100-KIN cells (WT 100% to 140%; KIN 60% to 88%), a finding which provides evidence that the transcriptional regulation of the knock-in allele is intact. As observed before, the expression levels of expanded *Atxn2* in *Atxn2*-CAG100-KIN cells were significantly lower than that of WT in both normal and adipogenic conditions (Fig. 7B). *Nat8l* transcript was not significantly different in *Atxn2*-CAG100-KIN cells under normal conditions. Upon adipogenesis in WT cells, *Nat8l* levels showed a big upregulation from 100% to 550%, proving once again the validity of adipogenic differentiation protocol and also the importance of *Nat8l* in this process. However, the transcriptional induction of *Nat8l* was completely repressed in *Atxn2*-CAG100-KIN cells upon adipogenic differentiation (Fig. 7B; KIN 98% to 150%), confirming a direct effect of ATXN2 expansion on the transcriptional regulation of *Nat8l* in cells outside the nervous system.

Finally, in order to test the effect of mutant ATXN2 on *Nat8l* in easily accessible peripheral tissues, and to establish an initial study for the molecular disease biomarkers, we analyzed abdominal adipose tissue from 3-month-old *Atxn2*-CAG100-KIN mice and blood samples from 14-month-old *Atxn2*-CAG100-KIN mice, as well as late symptomatic/terminal stage SCA2 patients. *Atxn2* transcript was significantly reduced in the adipose tissue to 64% ($p = .0456$), and *Nat8l* transcript was also significantly diminished to 58% ($p = .0110$; Fig. 7C). *Atxn2* transcript in blood samples of *Atxn2*-CAG100-KIN mice showed a significant decrease to 45% ($p = .0003$; Fig. 7D), similar to the previously shown expression deficit in *Atxn2*-CAG100-KIN MEFs. A dramatic decrease of *Nat8l* to 50% ($p = .0016$) was detected in *Atxn2*-CAG100-KIN mouse blood samples (Fig. 7D), further strengthening the direct effect of ATXN2 on *Nat8l* mRNA levels. Expression of *ATXN2* transcript in peripheral blood samples of four SCA2 patients and healthy controls showed higher variation compared to blood samples from *Atxn2*-CAG100-KIN mice (Fig. 7E). While two patients (#1 and #3) showed a decrease in *ATXN2* expression compared to their respective age- and sex-matched healthy controls, one patient (#4) showed no change, and one patient (#2) interestingly showed an increase in *ATXN2* expression. Measurement of *NAT8L* levels in SCA2 patient blood samples also revealed high variation among individuals of the same group; however, the comparison of *NAT8L* levels in each patient with the respective control consistently showed a decrease (44% on average) (Fig. 7E). Statistical analysis of the patient data with Ratio paired *t*-test revealed this consistent decrease in *NAT8L* levels to be significant (44%, $p = .0318$), but showed no significance for *ATXN2* expression changes (91%, $p = .5218$).

In conclusion, the magnetic resonance spectroscopy data from *Atxn2*-CAG100-KIN mouse cerebellum at 14 months and the expression analyses at different stages of the disease point to a NAA production deficit caused by dysregulated *Nat8l* expression, which starts very early at pre-symptomatic stages. Analyses in mouse primary fibroblasts under adipogenic treatment and in abdominal adipose tissue from mice, as well as blood samples from mice and patients corroborate this direct effect of expanded ATXN2 on *Nat8l* transcript reduction. Thus, *Nat8l* expression in blood is a candidate biomarker when assessing preventive treatments in SCA2.

3. Discussion

We generated a genetic mouse model of ATXN2 pathology, which faithfully reflects the spatial distribution of affected neural pathways with the preferential vulnerability of motor neurons, brainstem and cerebellar neurons resulting in chronically progressive locomotor deficits. The neurodegenerative process affects the nervous system with cytosolic inclusion bodies of ATXN2 in the characteristic pattern of olivo-ponto-cerebellar atrophy (OPCA), as was carefully documented in patients (Auburger, 2012; Estrada et al., 1999; Gierga et al., 2005; Hoche et al., 2011; Rub et al., 2006; Rub et al., 2004; Rub et al., 2005a; Rub et al., 2003a; Rub et al., 2005b; Rub et al., 2003b; Rub et al., 2007). The aggregates are particularly large in spinal motor neurons in our mouse model, and indeed it was recently shown in SCA2 mutation carriers that motor neuron degeneration appears even before the onset of cerebellar ataxia, accompanied by muscle cramps, impaired conduction velocity due to axon demyelination and the loss of subcutaneous fat tissue (Velazquez-Perez et al., 2001; Velazquez-Perez et al., 2014; Velazquez-Perez et al., 2016; Velazquez-Perez et al., 2017a). In good agreement with the early vulnerability of motor neurons and cerebellar circuits, the locomotor behavior data reflect a reduced performance on the accelerating rotarod from the age of 5 months, together with a steady decrease of peripheral grip strength from the age of 6–7 months onward, and balance problems during vertical movements in the open field from the age of 7 months. As the first knock-in model of SCA2 with shortened survival and endogenous regulation of ATXN2 expression and distribution, it will enable us to address the question to what degree loss-of-function effects e.g. in blood or fibroblasts exist in addition to the toxic gain-of-function effects that dominate in neural tissues. In this knock-in model it will also be possible to test substances that repress the transcription activity of the expanded *Atxn2* gene promoter. These issues cannot be answered in previously available transgenic overexpression models of SCA2.

Our initial observations regarding the gain- versus loss-of-function issue came from the phenotypic analyses of the mice throughout lifespan. Weight measurements showed an initial increase in female homozygous *Atxn2*-CAG100-KIN mice at pre-symptomatic stage, which progressively deteriorated and turned into a systemic tissue atrophy when locomotor deficits appeared. Considering that the most prominent phenotypic feature of *Atxn2*-KO mice is lipid accumulation and obesity, we suspected that this initial weight excess might be due to a partial loss-of-function effect caused by the mutant protein not being fully functional. Moreover, reduced number of female mutants and motor hyperactivity of the *Atxn2*-CAG100-KIN mice in early life also correlates well with the same phenotypes observed in *Atxn2*-KO animals reported previously (Lastres-Becker et al., 2008a). Interestingly, the change in body weight showing an initial increase followed by progressive decrease was not only observed in our mouse model, but also in SCA2 families upon careful longitudinal assessment (Abdel-Aleem and Zaki, 2008). Our further histological and biochemical studies showed the progressive aggregation of mutant ATXN2 protein in nervous tissue, and a strongly reduced abundance in peripheral tissues

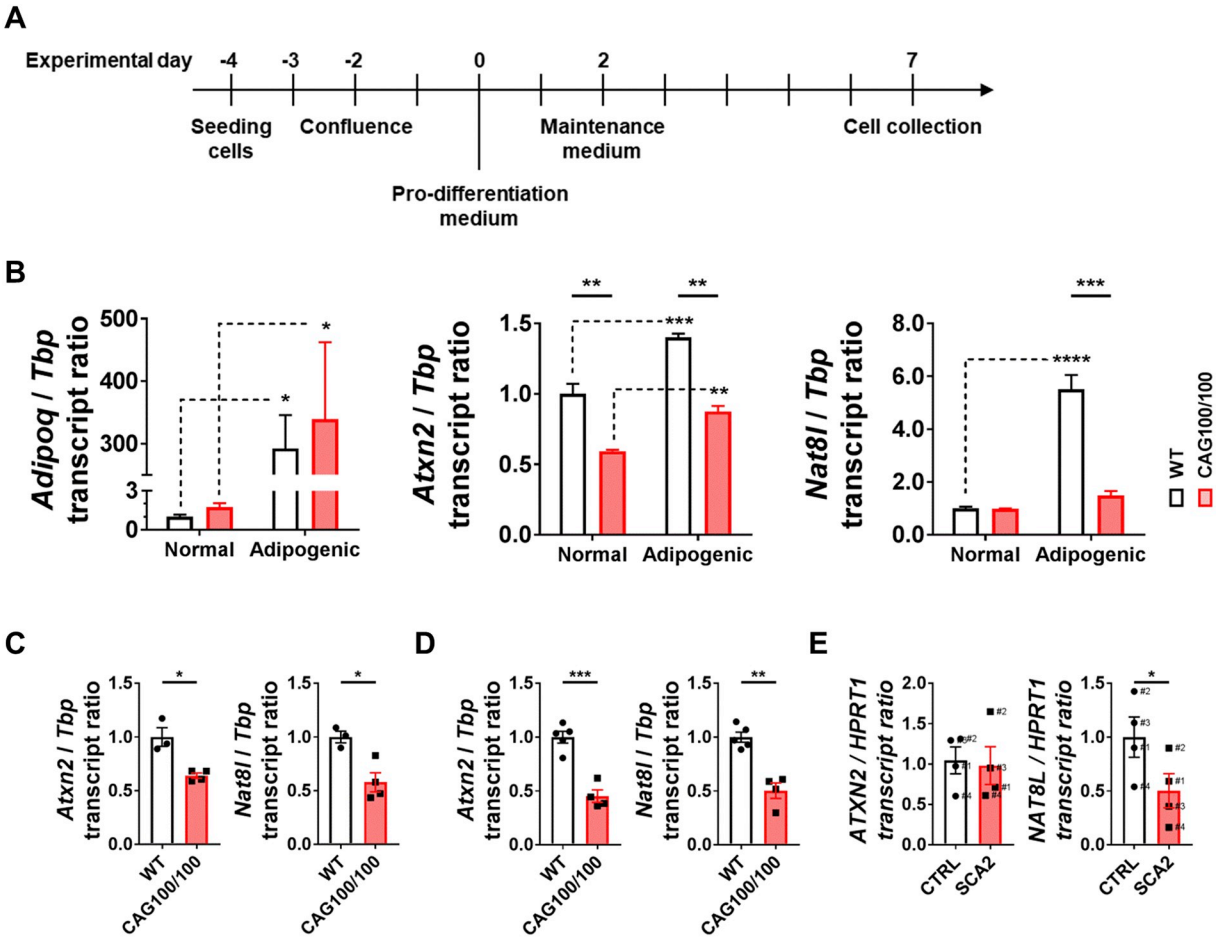

Fig. 7. *Nat8l* levels are modulated by mutant ATXN2 in adipogenic differentiation and blood. (A) Experimental timeline of MEF adipogenic differentiation protocol. (B) Expression analyses of *Adipoq* (Adiponectin, as a marker of adipogenesis), *Atxn2* and *Nat8l* in normal and adipogenic *Atxn2*-CAG100-KIN cells. Statistical analyses were done by Two-way ANOVA with Sidak's multiple test correction. Bar graphs show individual values together with mean ± s.e.m. (C) Expression analyses of *Atxn2* and *Nat8l* in *Atxn2*-CAG100-KIN white adipose tissue at the age of 3 months. Statistical analyses were done by unpaired t-test with Welch's correction. Bar graphs show individual values together with mean ± s.e.m. (D) Expression analyses of *Atxn2* and *Nat8l* in *Atxn2*-CAG100-KIN peripheral blood at the age of 14 months. Statistical analyses were done by unpaired t-test with Welch's correction. Bar graphs show individual values together with mean ± s.e.m. (E) Expression analyses of *ATXN2* and *NAT8L* in peripheral blood samples of SCA2 patients compared to age- and sex-matched healthy controls. Statistical analyses were done by Ratio paired t-test. Bar graphs show individual values together with mean ± s.e.m.

without aggregation. Similar findings of neurodegeneration with reduced levels and insolubility of polyQ expanded disease proteins were also reported for SCA7 (Helmlinger et al., 2004). For polyQ expanded Ataxin-3 it was shown that expression and solubility was normal in induced pluripotent stem cells, fibroblasts or glia cells, but changed to an insoluble aggregated state upon neuronal differentiation and exposure to excitatory stimuli such as glutamate (Koch et al., 2011). These previous observations explain our findings that ATXN2-CAG100 is quite soluble in fibroblasts, although severely decreased in abundance, while it appears to go into immediate insolubility and aggregation in neural tissue since pre-manifest stages.

After the initial weight excess, the progressive loss of body and also brain weight is compatible with the insidious increase of expanded ATXN2 toxicity due to aggregate formation. ATXN2 is expressed in pancreas and affects the islet beta-cells in their trophic state and insulin secretion (Lastres-Becker et al., 2008a), so we assume that aggregated ATXN2 toxicity affects these postmitotic cells via the known effects of ATXN2 on mTORC1 signaling and nutrient metabolism in general (Bar, 2016; DeMille et al., 2015; Lastres-Becker et al., 2016; Meierhofer, 2016; Seidel et al., 2017; Takahara and Maeda, 2012; Yang et al., 2019), thus triggering a depletion of body fat stores. Similarly, the observed strong weight reduction of the brain in *Atxn2*-CAG100-KIN mice might be explained largely by the loss of myelin fat. Very large *ATXN2* expansions in SCA2 patients clearly trigger myelination defects, since these patients develop widespread leukoencephalopathy observed upon brain imaging (Paciorkowski et al., 2011). The fact that expanded ATXN2 reduces *Nat8l* levels obviously may contribute to a decrease in myelin and brain weight. Moreover, the same pathomechanism might be partly responsible for the progressive atrophy of peripheral fat stores, as NAT8L has been reported as an important regulator of adipogenesis in white and brown adipose tissue (Huber et al., 2019; Kedersha and Anderson, 2007; Prokesch et al., 2016).

Aside from the pathological pattern and locomotor deficits, *Atxn2*-CAG100-KIN mice also reflect the metabolite profile documented in SCA2 patients previously in terms of decreased NAA, glutamate and choline levels (Cahill Jr. and Veech, 2003; Wang et al., 2012). This is similar to mouse models of other spinocerebellar ataxia types, such as SCA1 (Emery, 2005; Oz et al., 2015; Oz et al., 2011), where NAA levels were studied in parallel to histology to define the progression of neurodegeneration. NAA is the second most abundant metabolite in the brain after glutamate, and is predominantly synthesized in neurons via N-terminal acetylation of aspartate amino acid. Due to its high abundance and appearance as the largest peak in spectrograms, NAA deficiency has been widely used as a biomarker of neuronal loss or dysfunction in a number of neuropathological conditions, although it has never been clarified what is the underlying molecular mechanism of

this deficit (Cao et al., 2013b). It is well-established that the main purpose of NAA synthesis in the nervous system is to stock acetyl-CoA units in a transportable form for energy storage and acetylation reactions, which control gene expression and protein function. The only resident energy stores in the brain are small amounts of glycogen in astrocytes, so it is reasonable that the nervous system developed ways to ensure the interconversion of critical precursors for energy metabolism, such as glutamate and NAA that can easily be converted into α-ketoglutarate, acetate and oxaloacetate. It has been proposed that acetyl-CoA stored in the form of NAA in the CNS is the equivalent of triglycerides constituting the stored energy in the adipose tissue (Ariyannur et al., 2010). Indeed, our previous investigations on the physiological function of ATXN2 showed that yeast α-ketoglutarate dehydrogenase levels were affected by the loss of ATXN2. Also, fatty acid beta-oxidation and branched-chain amino acid degradation pathways within mitochondria were found severely affected by ATXN2 deficiency in mouse (Meierhofer, 2016; Seidel et al., 2017). Our current findings also point out to a mitochondrial enzyme, NAT8L, to be altered more than other NAA turnover enzymes, since earliest stages in the disease course and to a greater extent.

NAT8L was identified as the highly specialized *N*-acetyltransferase carrying out the synthesis of NAA. It is also involved in ATP-dependent axon growth and the inhibition of methamphetamine action by inducing dopamine uptake in nucleus accumbens (Della Nave et al., 2004; Faught, 2011). A single case carrying a 19 bp deletion mutation in *NAT8L* has been reported to have no detectable NAA peak in the NMR spectrogram, and to present with mild hypomyelination (Wang et al., 2012). This contrasts with Canavan disease (CD) where deleterious *ASPA* mutations lead to NAA accumulation in the brain, triggering severe progressive leukodystrophy and paralysis in infants and children (Jaeken et al., 1984). It was proposed that *NAT8L* dysfunction leads to a later and milder disease course compared to *ASPA* deficiency simply due to the availability of aspartate and acetate metabolites. On the one hand in CD, neurons utilize their aspartate and acetyl-CoA stores to synthesize NAA and transport it into oligodendrocytes. However, due to the lack of ASPA function, NAA cannot be broken down, myelination cannot occur and excess NAA is excreted from the CNS. This puts both oligodendrocytes and neurons into an energy deficit given that the main source of energy is constantly being pumped out to the blood. In *NAT8L* deficiency, on the other hand, aspartate and acetate molecules are not trapped in an un-degradable form, but rather NAA production simply does not occur. Both the neurons and oligodendrocytes can survive for a limited time utilizing other forms of energy stores, therefore myelination can take place, although at a decreased level (Ariyannur et al., 2010). This hypothesis correlates well with our findings that cerebellar NAA and *Nat8l* levels are significantly downregulated starting from pre-manifest stage, and decreasing with age. The deficit in *Aspa* levels later during disease progression may be a response to reduced *Nat8l* and NAA production, rather than being causative in disease manifestation.

In our spectroscopic data collection and analysis methodology, NAA and its downstream metabolite NAAG are visualized together within the same peak, and therefore are quantified together. NAAG is synthesized via the ATP-dependent condensation of NAA and glutamate. High levels of NAAG Synthase (NAAGS) and NAAG have been found in central nervous system, particularly spinal cord and brainstem, and in testis. In cerebellum, the highest expression of NAAGS occurs in Bergmann glia in the Purkinje cell layer. After its synthesis in neurons, NAAG is released from the synaptic terminals to act as a modulator of glutamatergic synapses, and excess NAAG is taken up and degraded by FOLH1 enzyme synthesized by astrocytes (Besse et al., 2015). It is known that ASPA deficiency leads to the accumulation of NAA and also NAAG in the CNS, however it is unknown how NAAG levels change in NAT8L deficiency, or in the context of many disorders with which NAA decrease was found to be associated. Quantification of the spectroscopic data acquired from *Atxn2*-CAG100-KIN cerebrum and cerebellum shows a consistent decrease in both tNAA and glutamate levels. The concentration of NAA in CNS is over 25 times higher than NAAG (Moffett and Namboodiri, 1995), and the detected tNAA peak is most probably dominated by NAA over NAAG. Nevertheless, it is reasonable to assume that NAAG levels must also be diminished in the mutant mice as the two building blocks, NAA and glutamate, were found significantly reduced.

In order to delineate the cause of NAA deficiency in *Atxn2*-CAG100-KIN mice, we have analyzed several important steps in NAA turnover at the molecular level and came to the conclusion that NAT8L is the earliest and strongest dysregulation. Then, we went on to analyze additional factors important in aspartate and acetyl-CoA turnover, hypothesizing that reduced availability of these metabolites in correct subcellular organelles might underlie the NAT8L reduction in response to impaired substrate levels. Among these factors, AGC1 (*Slc25a12*) was of special interest since it is the dominant cytoplasm/mitochondria aspartate transporter in brain, and its malfunction has been shown to cause global cerebral hypomyelination, severe hypotonia and seizures in infants (Broer and Palacin, 2011). AGC1 deficient mice also showed hypomyelination due to severely reduced aspartate levels and NAA synthesis, as also demonstrated in vitro (Broer and Palacin, 2011; Cao et al., 2013a). However, none of the factors including AGC1 showed a major dysregulation even at the terminal stage of the disease in *Atxn2*-CAG100-KIN mouse cerebellum, further strengthening our impression that NAT8L stands out as the main affected factor responsible for NAA deficiency in our mutant.

Both NAA and NAT8L have been widely studied in the context of nervous system metabolism and myelination. However, an additional role of NAT8L in regulating lipid metabolism outside the brain, namely in adipocytes, has been established rather recently. NAT8L expression was shown to be relatively high in white and brown adipose tissues and adipogenic cell lines, where it facilitates the balance between nutrient metabolism and lipolysis/lipogenesis (Huber et al., 2019; Kedersha and Anderson, 2007). In addition, acetyl-CoA released by the breakdown of NAA was shown to regulate histone acetylation, thus modulating the transcriptional profile of adipocytes by an epigenetic mechanism (Prokesch et al., 2016). Considering this vast importance of NAT8L in adipogenesis, we subjected primary MEF cells from WT and *Atxn2*-CAG100-KIN animals to an adipogenic differentiation regimen to test the effect of mutant ATXN2 on the transcriptional regulation of *Nat8l* in vitro. The induction of *Nat8l* in WT cells upon adipogenic differentiation was observed in line with the previous reports. Strikingly, this transcriptional induction was completely lost in *Atxn2*-CAG100-KIN cells under the same treatment. Likewise, a reduction of *Nat8l* transcript was observed in adipose tissue at the pre-symptomatic stage of 3 months in mutant mice. Additional analyses conducted with mutant mouse and SCA2 patient blood samples revealed a similar genotype effect at transcript level. The high variation of *ATXN2* and *NAT8L* transcript levels in human samples will be limiting for their use as molecular biomarkers of disease, but of course any out-bred population with a wide variability in nutrient intake and diverse environmental factors will always have a quite broad range of mRNA responses to stimuli and stress. In addition, the SCA2 patients analyzed in the framework of this study had smaller expansion sizes, but more advanced disease duration than our in-bred *Atxn2*-CAG100-KIN mice with minimum genetic, environmental or pathological differences. The applicability of these findings and the value of *NAT8L* as a disease marker remain to be validated in large SCA2 cohorts and in the context of other ATXN2-related disorders such as ALS or Parkinsonism syndromes.

Why is the *Nat8l* mRNA dysregulation observed early in peripheral adipose tissues of our mouse mutant, while the NAA deficits occur only later in cumulative manner in the nervous system? It is known from SCA2 patients that NAA reduction upon brain imaging and the ensuing demyelination indeed are late progression markers, while the loss of subcutaneous fat is a presymptomatic feature (Diallo et al., 2017; Medrano-Montero et al., 2018; Scherzed et al., 2012; Wang et al., 2012). When peripheral fat and protein stores are depleted by

malnutrition or atrophic disease, the overall brain is relatively spared from the general weight loss and logarithmically correlated to body weight, while myelin loss is linearly correlated to body size (Royland et al., 1992). Malnutrition is initially compensated by a rise in metabolic rates of liver/kidney glycogen to maintain energy supply to the brain via increased glycogenic activity, until the necessary protection of muscle mass triggers a switch to ketogenic breakdown of triglycerides stored in the adipose tissues (Emery, 2005). Ketone bodies help individuals with high body-mass-index to survive 3–4-fold longer starvation periods (Cahill Jr. and Veech, 2003). A higher body-mass-index lowers the risk to die from motor neuron diseases like ALS (Nakken, 2019). The relative sparing of brain neurons and the generation of NAA in the neuronal mitochondria may explain why the central nervous system shows later disease manifestation in SCA2 than the subcutaneous fat stores. If this delay can be exploited to replete body stores of fat via hypercaloric diets, then it may become possible to postpone or mitigate the neurodegeneration, as already shown for ALS (Wills et al., 2014).

In conclusion, an authentic mouse model of SCA2 has been generated that mirrors numerous aspects of disease pathology, motor deficit and metabolic alterations without the potential off-target effects of an over-expression or transgenic strategy. It offers unique opportunities to accurately elucidate molecular mechanisms in a tissue- and cell-specific manner. Moreover, it represents an excellent tool for the development of molecular biomarkers in the assessment of disease progression or the effect of therapeutic manipulations. Overall, the molecular findings presented here provide insights into very early disease stages, where future curative therapies have to be applied and assessed.

4. Materials and methods

4.1. Generation of Atxn2-CAG100 knock-in mice

For the generation of *Atxn2*-CAG100 knock-in (KIN) mice we modified the previously described pKO-*Sca2*-vector (Lastres-Becker et al., 2008a). The existing targeting construct had additional restriction sites inserted to permit the Southern blot analysis of Flp-mediated excision events, then the exon 1 region was modified between the unique restriction sites Eco47III and *Sgr*AI with the insertion of a CAG100 repeat (custom-made by GeneArt, Regensburg) at position Q156 and with the G > A creation of an additional *Sph*I restriction site 422 basepairs (bp) upstream the CAG repeat without alteration of the amino acid sequence, naming the modified vector NOW1-HR. The instability of large CAG repeats in bacteria was restrained by using the recombination-deficient SURE strain (Stratagene, now Agilent, Santa Clara) of *E. coli* bacteria and cultured at 30 °C for several hours on LB medium plates. Sequence verification of individual clones and *Sac*II digestion to control expansion length were performed before electroporating Kpn1 linearized vector into *Mus musculus* 129Sv/Pas strain embryonal stem (ES) cells to allow for homologous recombination at the endogenous *Atxn2* locus. The integration was confirmed in 6 ES cell clones as described previously (Damrath et al., 2012), employing the strategy depicted in Fig. 1A and the primers detailed in Table S1. Flp mediated excision was used to remove the neomycin resistance cassette. One correctly targeted ES cell line with verified expansion length of CAG100 was injected into *Mus musculus* C57BL/6 strain blastocysts. This work was outsourced to Genoway (Lyon, France).

4.2. Animals

All animals were housed at the Central Animal Facility (ZFE) of the Goethe University Medical School, Frankfurt am Main, at mfd Diagnostics GmbH in Wendelsheim, Germany, FELASA-certified facility. They were kept in individually ventilated cages at a 12 h-light/12 h-dark cycle under routine health monitoring and fed *ad libitum*. All procedures were in accordance with the German Animal Welfare Act, the Council Directive of 24th November 1986 (86/609/EWG) with Annex II and the ETS123 (European Convention for the Protection of Vertebrate Animals). Mice were backcrossed from a mixed 129Sv/Pas × C57BL/6 strain for at least 8 generations into the C57BL/6 strain. Heterozygous mating was employed. Among offspring littermates, the homozygous *Atxn2*-CAG100-KIN and WT animals of the same sex were selected and aged in neighboring cages for subsequent case-control comparisons in neuropathology and expression studies. Sperm cryopreservation was carried out at Genoway (Lyon, France) and the mice will in due course be made available through the EMMA mouse repository, where the *Atxn2*-CAG42-KIN line is already available, see https://www.infrafrontier.eu/search.

4.3. Genotyping of Atxn2-CAG100-KIN mice

DNA was isolated from ear punches and the genotyping PCR was performed. TaKaRa LA Taq-Polymerase (Takara Bio Inc., Japan) was used to amplify the neomycin cassette excised locus with the primer pair NOW1-K2 5′-TGAGTTGACTCCACAGGGAGGTGAGC-3′ and NOW1-H2 5′-CCATCTCGCCAGCCCGTAAGATTC-3′ flanking this site. The conditions were: initial denaturation at 94 °C for 3′, followed by 30 cycles of denaturation at 94 °C for 15″, annealing at 68 °C for 4′, elongation at 68 °C for 4′, and a final elongation step at 68 °C for 9′. The wild-type (WT) allele is predicted to yield an amplification product of 793 bp and the CAG100 allele of 948 bp. For amplification of the CAG repeat, the primers Sca2Ex1_Fwd5 5´-CCCCGCCCGGCGTGCGAGCCGG TGTAT-3′ and Sca2Ex1_Rev2 5´-CGGGCTTGCGGCCAGTGG-3′ were used. CAG100 allele has a predicted length of 387 bp, while WT allele has 90 bp. Initial denaturation at 98 °C for 3′, followed by 39 cycles of denaturation at 98 °C for 40″, annealing at 60 °C for 40″, elongation at 72 °C for 1′ and a final elongation step at 72 °C for 7′ was used. For exact sizing by fragment length analysis, these PCR products were purified with the QIAquick PCR Purification Kit. Samples were processed in 96 well plates on an Applied Biosystems 3730 DNA analyzer (StarSEQ GmbH, Mainz), sizing the peaks in comparison to a Genescan 500 LIZ standard and analyzing the electropherogram with the Peak Scanner 2.0 software as previously reported (Gispert et al., 2012).

4.4. Body weight and behavioral observations

Offspring with WT or CAG1/100 and CAG100/100 genotype of similar ages and identical sex were used as case-control pairs for phenotypic comparisons. Sudden death of animals was documented together with the relevant age information. Mice were weighed before behavioral testing. In contrast to all other measurements, male and female animals were separated for weight analyses due to strong gender-specific weight differences. Brain weight was measured after cervical dislocation, dissection and removal of the olfactory bulb, employing an analytical balance. If not otherwise stated, male and female animals were used for phenotype studies without separation. Grip strength was assessed by measuring the peak force of the fore limbs in 10 trials per mouse on an electronic grip strength meter (TSE, Bad Homburg). Paw prints were evaluated by painting the forepaws with a non-toxic red ink, the hind limbs of mice with blue. The mice were placed at one end of a dark tunnel, so that their walk to the other end will leave paw prints on the white paper that covers the floor (tunnel 6 cm high × 9 cm wide × 40 cm long). Footprint movement patterns were analyzed as described previously (Damrath et al., 2012). Assessment on an accelerating rotarod apparatus (model 7650 Robert & Jones, Ugo Basile, Comerio) and in an open field arena (Versamax, Omnitech, Columbus, Ohio) were performed as previously described (Damrath et al., 2012). During the acceleration of the rotarod from 4 to 40 rpm, every mouse had four consecutive 6 min trials interrupted by at least 10 min of break without previous training. The latency to fall was recorded for each trial; the mean value of the four trails was calculated and used for statistical analysis. Video recording occurred at ages from

10 to 14 months. For the beam test, the animals had to walk across a surface with length of ~1 m and a diameter of 18 mm. For the clasping test mice were suspended by their tails for about 1 min. Behavioral analyses were always conducted at the same daytime to avoid variances caused by circadian rhythm.

4.5. Generation of murine embryonal fibroblasts, cell culture and treatments

Primary murine embryonal fibroblast (MEF) cultures were generated from wild type (WT) and homozygous *Atxn2*-CAG100-KIN embryos around E15–18 as described earlier (Lastres-Becker et al., 2016). Culture preparation medium consisted of high glucose DMEM (Gibco), 15% BS (PAA Cell Culture Company), 1× L-glutamine (Gibco) and 2× Penicillin-Streptomycin (Gibco). Medium was changed daily for the first three days. Once confluent, the cells were transferred into a T25 flask and were cultured in growth medium (high glucose DMEM, 15% BS, 1× L-glutamine, 1× Penicillin-Streptomycin).

For RNA and protein isolation, WT and *Atxn2*-CAG100-KIN MEF cultures were grown to confluency, and cell pellets were obtained by scraping and centrifugation. For immunocytochemistry, cells were trypsinized and counted. 5×10^4 cells were seeded on 12 mm cover slips. 24 h after seeding, cells were washed with PBS and the medium was replaced with either normal growth medium or growth medium supplemented with 0.5 mM sodium arsenite (NaARS, Sigma) for 45 min. Then, the medium was aspirated and cells were washed with PBS before fixation for immunocytochemistry (see below). For puromycin incorporation analysis, 50×10^5 cells were seeded on 6-well plates the day before experiment. Puromycin (Santa Cruz) at the final concentration of 5 μM was added to the culture medium for 20 min, after which cells were washed with PBS, scraped and centrifuged to obtain the cell pellet.

4.6. Adipogenic differentiation of MEFs

Adipogenic differentiation of WT and *Atxn2*-CAG100-KIN MEFs was performed as reported (Zhang et al., 2009), and as depicted in Fig. 7A. Briefly, 5×10^5 cells were seeded in 6-well plates and grown in normal MEF culture medium described above, 1–2 days later confluency was achieved. Two days post-confluency, culture medium was replaced with pro-differentiation medium [normal culture medium supplemented with 830 nM insulin (Sigma), 1 μM dexamethasone (Cayman Chemicals), 0.5 mM 3-isobutyl-1-methylxanthine (IBMX, Cayman Chemicals), and 5 μM troglitazone (Cayman Chemicals)]. Two days later pro-differentiation medium was replaced with maintenance medium [normal culture medium supplemented with 830 nM insulin]. Maintenance medium was replaced every two days until harvest on Day 7. Control cells without adipogenic differentiation were seeded in parallel and were collected on Day 0 for expression analyses.

4.7. Nuclear and cytoplasmic fractionation of cerebellum

After cervical dislocation, whole brain was removed and cerebellum was dissected. Half of fresh cerebellum was homogenized in Hypotonic Nuclear Extraction (HNE) Buffer [100 mM NaCl, 50 mM Tris-HCl pH 7.4, 10 mM $MgCl_2$, 1% Triton-X, 40 U/ml RNaseOUT (Invitrogen)], with a motor pestle. After rotation at 4 °C for 10 min, and centrifugation at 1000 ×*g* for 10 min at 4 °C, supernatant was collected into a new tube as "cytoplasmic" fraction and was frozen. The pellet was washed 2× in cold HNE buffer and centrifuged, the final pellet consisting of the "nuclear" fraction was frozen until further processing.

4.8. RNA isolation and expression analysis

Whole brain was removed after cervical dislocation; cerebellum and two hemispheres were dissected into separate tubes and immediately frozen in liquid nitrogen. Abdominal adipose tissue was collected and frozen in liquid nitrogen. RNA extraction from cerebellum, adipose tissue and cultured cells was performed with TRIzol Reagent (Sigma Aldrich) according to user manual. Collection of blood samples from SCA2 patients and age- and sex-matched controls after overnight fasting, and processing of the blood samples has been described previously (Sen et al., 2016). RNA isolation from total blood with PAXgene Blood RNA Kit (Qiagen) was performed according to manufacturer's instructions. Total blood samples from mice was collected via cardiac withdrawal into EDTA tubes and frozen until processed. RNA isolation from mouse blood samples was performed with TRI Reagent BD (Sigma Aldrich) according to manufacturer's instructions.

Synthesis of cDNA from 1 μg of total RNA template was performed by the SuperScript IV VILO kit (ThermoFisher) according to manufacturer's instructions. The expanded *Atxn2* transcript was amplified from cerebellar cDNA with RT-PCR using primers flanking the CAG site and was assessed in a 2% agarose gel. To assess the gene expression changes, quantitative real-time PCR analyses were performed with StepOnePlus Real-Time PCR System (Applied Biosystems) equipment. cDNA from 25 ng total RNA was used for each PCR reaction with 1 μl TaqMan® Assay, 10 μl FastStart Universal Probe Master 2× (Rox) Mix and ddH_2O up to 20 μl of total volume. The mouse specific TaqMan® Assays utilized for this study are: *Aspa* (Mm00480867_m1), *Atxn2* (Mm01199894_m1), *Cs* (Mm00466043_m1), *Folh1* (Mm00489655_m1), *Got1* (Mm01195792_g1), *Got2* (Mm00494703_m1), *Nat8l* (Mm01217217_m1), *Slc25a1* (Mm00467666_m1), *Slc25a11* (Mm00455209_m1), *Slc25a12* (Mm00552464_m1), *Slc25a13* (Mm00489442_m1) and *Tbp* (Mm00446973_m1). The human specific TaqMan® Assays utilized for this study are: *ATXN2* (Hs00268077_m1), *NAT8L* (Hs00402258_m1) and *HPRT1* (Hs99999909-m1). The PCR conditions were 50 °C for 2 min, 95 °C for 10 min, followed by 40 cycles of 95 °C for 15 s and 60 °C for 1 min. U2 snRNA (*Rnu2*) and *Actb* levels were analyzed with SYBR Green primers (U2-Forward: 5'-CTCGGCCTTTTGGCTAAGAT-3′, U2-Reverse: 5'-CGTTCCTGGAGGTACTGCAA-3′, *Actb*-Forward: 5'-GGAAATCGTGCG TGACATCAAAG-3′, *Actb*-Reverse: 5'-CATACCCAAGAAGGAAGGC TGG-3′) in a reaction of cDNA from 25 ng total RNA, 5 pmole/μl primers, 10 μl qPCR Mastermix Plus for SYBR Green I (Eurogentec) and ddH_2O up to 20 μl of total volume. The PCR conditions were 95 °C for 10 min, followed by 40 cycles of 95 °C for 15 s and 60 °C for 1 min and a melt curve stage of 95 °C for 15 s, 60 °C for 1 min and 95 °C for 15 s. Gene expression data was analyzed using $2^{-\Delta\Delta Ct}$ method (Livak and Schmittgen, 2001) with *Tbp*, *Actb* and *HPRT1* as housekeeping genes.

4.9. Protein extraction and western blots

Cerebellar tissue was homogenized with a motor pestle in 5-10× weight/volume amount of either PN buffer [PBS, 1% NP-40, 150 mM NaCl] or RIPA buffer [50 mM Tris-HCl (pH 8.0), 150 mM NaCl, 2 mM EDTA, 1% Igepal CA-630 (Sigma), 0.5% sodium deoxycholate, 0.1% SDS and Complete Protease Inhibitor Cocktail (Roche)]. Following centrifugation, the PN buffer pellets were dissolved in Urea buffer [8 M Urea, 10 mM tris(2-carboxyethyl)phosphine hydrochloride (TCEP, Carl Roth), 40 mM 2-chloroacetamide (2-CAA, Sigma Aldrich), 100 mM Tris-HCl and Complete Protease Inhibitor Cocktail (Roche)] in order to obtain insoluble proteins. Cell pellets from MEF cultures were homogenized in RIPA buffer. Protein concentration was determined with a Spectrophotometer (Eppendorf) using 5× Bradford Reagent (Roti-Quant, Carl Roth). 20 μg of total proteins were mixed with 2× loading buffer [250 mM Tris-HCl pH 7.4, 20% Glycerol, 4% SDS, 10% 2-Mercaptoethanol, 0.005% Bromophenol blue], incubated at 90 °C for 2 min, separated on polyacrylamide gels and were transferred to Nitrocellulose membranes (GE Healthcare). The membranes were blocked in 5% BSA/TBS-T, and incubated overnight at 4 °C with primary antibodies against ASPA (Thermo Fischer, PA5–29180), ACTB (Sigma #A5441, 1:10000), ATXN2 (Proteintech #21776–1-AP), GOT2 (Acris #AM06383SU-N, 1:500), NAT8L (Abbexa, abx431860), PABP (Abcam ab21060), Puromycin (Merck Millipore, MABE343), SLC25A12

(AGC1) (abcam, ab200201), TUBA (abcam, ab-15246). Fluorescently labeled secondary goat anti-mouse (IRDye 800CW, Li-Cor, 1:10,000) and goat anti-rabbit (IRDye 680RD, Li-Cor, 1:10000) antibodies were incubated for 1 h at room temperature. Membranes were visualized using Li-Cor Odyssey Classic instrument. The image analysis to quantify signal intensities was performed using ImageStudio software.

4.10. Perfusion

Mice were anesthetized with an overdose of Ketaset (300 mg/kg) and Domitor (3 mg/kg) by an intraperitoneal injection. To assess the anesthetic depth, the withdrawal reflex was monitored. Intracardial perfusion was done with phosphate buffer saline (PBS) followed by 4% paraformaldehyde (PFA) in 0.1 M PBS. For paraffin embedded sections, the tissue was post-fixed overnight in 4% PFA at 4 °C, dehydrated and incubated in paraplast for 24 h at 56 °C. All tissues were cut and mounted in 7 µm-thick slices using a microtome. For cryosections, the tissue was also post-fixed overnight in 4% PFA at 4 °C, immersed in 30% sucrose until it sank, cut with a cryostat in 30 µm-thick slices and kept in cryoprotection solution (30% ethylene glycol, 25% glycerin, 0.01% sodium azide in 0.1 M PBS) at −20 °C until used.

4.11. Histology and immunostaining

For immunocytochemistry, 5×10^4 cells from WT and *Atxn2*-CAG100-KIN MEF cultures were seeded on 12 mm cover slips. Next day, the cells were washed and stressed with 0.5 mM NaARS supplemented in the DMEM growth medium for 45 min at 37 °C. Control cells were washed and supplemented with only DMEM growth medium for 45 min. Cells were washed once before fixation with 4% paraformaldehyde/PBS at room temperature (RT) for 20 min, then were permeabilized with 0.1% Triton-X-100/PBS for 20 min at RT. Blocking was done with 3% BSA/PBS solution for 1 h at RT. Primary antibody incubation with PABP (Abcam ab21060, 1:100) and ATXN2 (BD Biosciences #611378, 1:100) antibodies was performed in 3% BSA/PBS for 1 h at RT. Secondary antibody incubation with goat anti-rabbit-Alexa Fluor 546 (Molecular Probes, 1:1000), goat anti-mouse-Alexa Fluor 488 (Molecular Probes, 1:1000) antibodies and DAPI was performed in 3% BSA/PBS for 1 h at RT in dark. The coverslips were mounted on glass slides with fluorescent mounting medium (Thermo Fisher) and dried overnight. Cell imaging was performed using Zeiss Axiovert 200 M inverted microscope using a 100 × objective, and ImageJ software was used to merge images.

For immunohistochemistry, paraffin embedded sections were rehydrated in a descending alcohol series. Bull's Eye Decloaker (1:20) was used for antigen retrieval and the sections were incubated with the following primary antibodies overnight: anti-1C2 (Millipore #MAB1574, 1:800), anti-ATXN2 (BD Bioscience #611378, 1:50), anti-p62 (Santa Cruz #sc25575, 1:50) and anti-Ubiquitin (UBQ, Dako #ZO458, 1:100). For DAB stainings, Vector NovaRED Peroxidase kit was used after blocking the endogenous peroxidase with 100% methanol, 30% H_2O_2 in Tris/HCl pH 7.6 (1:1:18) for 30 min. For fluorescent stainings, goat anti-rabbit-Alexa Fluor 546 (Molecular Probes, 1:1000), goat anti-mouse-Alexa Fluor 488 (Molecular Probes, 1:1000) antibodies and DAPI was used for 1 h at RT in dark. The Leica 090–135-001 microscope was utilized for single immunohistochemical stainings at magnitude 60×. Double immunofluorescence stainings with anti-ATXN2 (BD Bioscience #611378, 1:50) and PABP (Abcam ab21060, 1:250) was performed on free-floating cryosections. Secondary antibodies goat anti-mouse Alexa Fluor 488 (Molecular Probes, 1:1000), goat anit-rabbit Alexa Fluor 568 (Molecular Probes, 1:1000) and DAPI were incubated. Imaging was done with the confocal microscope Nikon eclipse TE2000-E at 40× magnification.

4.12. 1H-MR spectroscopy and data analysis

MR spectroscopy was performed using a 7 Tesla Small Animal MR Scanner (PharmaScan, Bruker, Ettlingen, Germany) with a volume coil as transmitter and a head surface coil for signal reception. Data were acquired with the Paravision 6.0.1 software. For MR scans, mice were anesthetized with isoflurane (2%) and stabilized in the prone position with a tooth holder. Body temperature was maintained at 36–37 °C with a built-in animal waterbed (Bruker, Ettlingen, Germany). Respiration rate was monitored and kept constant at 80–100 breaths per minute continuously throughout the measurement. For identifying the target areas on T2-weighted images, a localized T2-multislice Turbo rapid acquisition with relaxation enhancement was acquired (T2 TurboRARE; TE/TR = 33 ms/2500 ms, FOV = 20 × 20 mm, 11 slices, 0.5 mm slice thickness, acquisition matrix = 256 × 256, flip angle 90°). Single voxel spectroscopy (SVS) was performed using the point resolved spectroscopy sequence (PRESS) with an echo time (TE) of 16.5 ms, a repetition time (TR) of 2500 ms, spectral width of 3301.6 Hz and 2048 points data size. One voxel of 3 mm × 3 mm × 3 mm was placed in the cerebrum as indicated in Fig. 5A and 64 acquisitions were averaged in approximately 3 min. Another voxel of 2 mm × 2 mm × 2 mm was placed in the cerebellum and 256 acquisitions were averaged in approximately 12 min. The target selection was based on T2-weighted MRI data from the imaging protocol. The volume of interest (VOI) was selected to contain only brain tissue without interference of the skull. For each measurement, homogeneity after shimming, measured as the full width at half maximum (FWHM) of the water peak was below 25 Hz. MR spectroscopic data was processed using the java-based MR user interface spectroscopic analysis package (jMRUI version 5.2) employing AQSES (Automated Quantification of Short Time Echo MRS), a time domain quantification method with which the residual water component could be filtered during the post-processing. Additionally, Cramer Rao lower bounds (CRLBs) of the metabolites of interest could be obtained from the quantification procedure. The following metabolites were included in the analysis: alanine (Ala), aspartate (Asp), ascorbate/vitamin C (Asc), glycerophosphocholine (GPC), phosphocholine (PCho), creatine (Cr), phosphocreatine (PCr), glucose (Glc), glutamine (Gln), glutamate (Glu), glutathione (GSH), glycine (Gly), myo-inositol (myo-Ins), lactate (Lac), *N*-acetylaspartate (NAA), *N*-acetylaspartylglutamate (NAAG), phosphoethanolamine (PE), scyllo-inositol (scyllo-Ins) and taurine (Tau). The respective basis data sets were generated by quantum-mechanical simulation using NMR-SCOPE-B, which is provided in the jMRUI package. Chemical shifts and scalar coupling constants were obtained from the literature (Govindaraju et al., 2000). Based on literature, the following terms were defined to determine aggregated values for metabolites that are difficult to separate from each other: tCho = GPC + PCho, tCr = PCr + Cr, tNAA = NAA + NAAG.

4.13. Electron microscopy

The tissue samples were fixed overnight using 2.5% glutaraldehyde buffered in cacodylate. The embedding procedure comprised fixation in 1% osmium tetroxide, dehydration in a graded ethanol series intermingled by an incubation step with uranyl acetate (between the 50% and 90% ethanol step) and finally rinsing in propylene oxide. The specimens were then embedded in epoxy resins that polymerized for 16 h at 60 °C. After embedding, first semi-thin sections (0.5 µm) were cut using an ultramicrotome (Leica Ultracut UCT, Deerfield, IL, USA) with a diamond knife. Sections were stained with Toluidine blue, placed on glass slides and examined by light microscopy to select appropriate areas for ultrathin preparation. Ultrathin sections (50–70 nm) were cut again using an ultramicrotome. Sections were mounted on copper grids and contrasted with uranyl acetate for 2–3 h at 42 °C and lead citrate for 20 min at RT. These samples were imaged and digital pictures were taken with a FEI Tecnai G2 Spirit Biotwin TEM (Hillsboro, OR) at an operating voltage of 120 kV.

4.14. Statistical analyses

Unless specified otherwise, all statistical tests were performed as unpaired Student's *t*-test with Welch's correction using GraphPad Prism software version 4.03 (2005) after establishing that each population was normally distributed (one-sided Kolmogorov-Smirnov test). Figures display mean values and standard error of the mean (s.e.m.). Values $p < .05$ were considered significant and marked with asterisks $^{*}p < .05$, $^{**}p < .01$, $^{***}p < .001$, $^{****}p < .0001$.

Supplementary data to this article can be found online at https://doi.org/10.1016/j.nbd.2019.104559.

Acknowledgements

The authors wish to thank Gabriele Köpf for technical assistance, and the staff at the Zentrale Forschungs-Einrichtung at Frankfurt University Medical School for their assistance with animal assessments.

Competing interests

No competing interests declared.

Funding

This work was supported by the Deutsche Forschungs-Gemeinschaft [AU 96/11-1, 113], the European Research Council Starting Grant [ERC-Stg, 680235] (MSc), the Netherlands Organization for Scientific Research (NWO-ALW; CIDZ), the Dutch Organization for Medical Sciences (ZonMW; CIDZ), Life Sciences (CIDZ), and ERC-adv and ERC-POC (CIDZ), and the Max Planck Society. Michel Mittelbronn would like to thank the Luxembourg National Research Fund (FNR) for the support [FNR PEARL P16/BM/11192868 grant].

References

Abdel-Aleem, A., Zaki, M.S., 2008. Spinocerebellar ataxia type 2 (SCA2) in an Egyptian family presenting with polyphagia and marked CAG expansion in infancy. J. Neurol. 255, 413–419.
Almaguer-Mederos, L.E., et al., 2010. Estimation of the age at onset in spinocerebellar ataxia type 2 Cuban patients by survival analysis. Clin. Genet. 78, 169–174.
Almaguer-Mederos, L.E., et al., 2013. Estimation of survival in spinocerebellar ataxia type 2 Cuban patients. Clin. Genet. 83, 293–294.
Al-Ramahi, I., et al., 2007. dAtaxin-2 mediates expanded Ataxin-1-induced neurodegeneration in a *Drosophila* model of SCA1. PLoS Genet. 3, e234.
Antenora, A., et al., 2018. Predictors of survival in spinocerebellar ataxia type 2 population from southern Italy. Neurol. Sci. 39, 1857–1860.
Ariyannur, P.S., et al., 2008. N-acetylaspartate synthesis in the brain: mitochondria vs. microsomes. Brain Res. 1227, 34–41.
Ariyannur, P.S., et al., 2010. Methamphetamine-induced neuronal protein NAT8L is the NAA biosynthetic enzyme: implications for specialized acetyl coenzyme A metabolism in the CNS. Brain Res. 1335, 1–13.
Auburger, G.W., 2012. Spinocerebellar ataxia type 2. Handb. Clin. Neurol. 103, 423–436.
Auburger, G., et al., 1990. Autosomal dominant ataxia: genetic evidence for locus heterogeneity from a Cuban founder-effect population. Am. J. Hum. Genet. 46, 1163–1177.
Auburger, G., et al., 2014. 12q24 locus association with type 1 diabetes: SH2B3 or ATXN2? World J. Diabetes 5, 316–327.
Auburger, G., et al., 2017. Efficient prevention of neurodegenerative diseases by depletion of starvation response factor Ataxin-2. Trends Neurosci. 40, 507–516.
Bar, D.Z., et al., 2016. Cell size and fat content of dietary-restricted *Caenorhabditis elegans* are regulated by ATX-2, an mTOR repressor. Proc. Natl. Acad. Sci. U. S. A. 113, E4620–E6429.
Becker, L.A., et al., 2017. Therapeutic reduction of ataxin 2 extends lifespan and reduces pathology in TDP-43 mice. Nature 544, 367–371.
Besse, A., et al., 2015. The GABA transaminase, ABAT, is essential for mitochondrial nucleoside metabolism. Cell Metab. 21, 417–427.
Broer, S., Palacin, M., 2011. The role of amino acid transporters in inherited and acquired diseases. Biochem. J. 436, 193–211.
Cahill Jr., G.F., Veech, R.L., 2003. Ketoacids? Good medicine? Trans. Am. Clin. Climatol. Assoc. 114, 149–161 (discussion 162-3).
Cancel, G., et al., 1997. Molecular and clinical correlations in spinocerebellar ataxia 2: a study of 32 families. Hum. Mol. Genet. 6, 709–715.
Cao, J., et al., 2013a. GABA transaminases from Saccharomyces cerevisiae and *Arabidopsis thaliana* complement function in cytosol and mitochondria. Yeast 30, 279–289.
Cao, J., et al., 2013b. GABA shunt mediates thermotolerance in *Saccharomyces cerevisiae* by reducing reactive oxygen production. Yeast 30, 129–144.
Ciosk, R., et al., 2004. ATX-2, the C. elegans ortholog of ataxin 2, functions in translational regulation in the germline. Development 131, 4831–4841.
Damrath, E., et al., 2012. ATXN2-CAG42 sequesters PABPC1 into insolubility and induces FBXW8 in cerebellum of old ataxic knock-in mice. PLoS Genet. 8, e1002920.
Dansithong, W., et al., 2015. Ataxin-2 regulates RGS8 translation in a new BAC-SCA2 transgenic mouse model. PLoS Genet. 11, e1005182.
Della Nave, R., et al., 2004. ADC mapping of neurodegeneration in the brainstem and cerebellum of patients with progressive ataxias. NeuroImage 22, 698–705.
Dell'Orco, J.M., et al., 2017. Potassium channel dysfunction underlies Purkinje neuron spiking abnormalities in spinocerebellar ataxia type 2. Hum. Mol. Genet. 26, 3935–3945.
DeMille, D., et al., 2015. PAS kinase is activated by direct SNF1-dependent phosphorylation and mediates inhibition of TORC1 through the phosphorylation and activation of Pbp1. Mol. Biol. Cell 26, 569–582.
Di Fabio, R., et al., 2012. Infantile childhood onset of spinocerebellar ataxia type 2. Cerebellum 11, 526–530.
Diallo, A., et al., 2017. Body mass index decline is related to spinocerebellar Ataxia disease progression. Mov. Disord. Clin. Pract. 4, 689–697.
Drost, J., et al., 2013. Ataxin-2 modulates the levels of Grb2 and SRC but not ras signaling. J. Mol. Neurosci. 51, 68–81.
Elden, A.C., et al., 2010. Ataxin-2 intermediate-length polyglutamine expansions are associated with increased risk for ALS. Nature 466, 1069–1075.
Emery, P.W., 2005. Metabolic changes in malnutrition. Eye 19, 1029–1034.
Estrada, R., et al., 1999. Spinocerebellar ataxia 2 (SCA2): morphometric analyses in 11 autopsies. Acta Neuropathol. 97, 306–310.
Faught, E., 2011. Vigabatrin therapy for refractory complex partial seizures: review of clinical trial experience in the United States. Acta Neurol. Scand. 29–35 Supplementum.
Fittschen, M., et al., 2015. Genetic ablation of ataxin-2 increases several global translation factors in their transcript abundance but decreases translation rate. Neurogenetics 16, 181–192.
Fleischer, T.C., et al., 2006. Systematic identification and functional screens of uncharacterized proteins associated with eukaryotic ribosomal complexes. Genes Dev. 20, 1294–1307.
Freund, H.J., et al., 2007. Subthalamic-thalamic DBS in a case with spinocerebellar ataxia type 2 and severe tremor-a unusual clinical benefit. Mov. Disord. 22, 732–735.
Gierga, K., et al., 2005. Involvement of the cranial nerves and their nuclei in spinocerebellar ataxia type 2 (SCA2). Acta Neuropathol. 109, 617–631.
Gispert, S., et al., 2012. The modulation of amyotrophic lateral sclerosis risk by ataxin-2 intermediate polyglutamine expansions is a specific effect. Neurobiol. Dis. 45, 356–361.
Giuffrida, S., et al., 1999. Supratentorial atrophy in spinocerebellar ataxia type 2: MRI study of 20 patients. J. Neurol. 246, 383–388.
Govindaraju, V., et al., 2000. Proton NMR chemical shifts and coupling constants for brain metabolites. NMR Biomed. 13, 129–153.
Guerrini, L., et al., 2004. Brainstem neurodegeneration correlates with clinical dysfunction in SCA1 but not in SCA2. A quantitative volumetric, diffusion and proton spectroscopy MR study. Brain J. Neurol. 127, 1785–1795.
Halbach, M.V., et al., 2015. Both ubiquitin ligases FBXW8 and PARK2 are sequestrated into insolubility by ATXN2 PolyQ expansions, but only FBXW8 expression is dysregulated. PLoS One 10, e0121089.
Halbach, M.V., et al., 2017. Atxn2 knockout and CAG42-knock-in cerebellum shows similarly dysregulated expression in calcium homeostasis pathway. Cerebellum 16, 68–81.
Hansen, S.T., et al., 2013. Changes in Purkinje cell firing and gene expression precede behavioral pathology in a mouse model of SCA2. Hum. Mol. Genet. 22, 271–283.
Heck, M.V., et al., 2014. Dysregulated expression of lipid storage and membrane dynamics factors in Tia1 knockout mouse nervous tissue. Neurogenetics 15, 135–144.
Helmlinger, D., et al., 2004. Disease progression despite early loss of polyglutamine protein expression in SCA7 mouse model. J. Neurosci. 24, 1881–1887.
Hoche, F., et al., 2011. Spinocerebellar ataxia type 2 (SCA2): identification of early brain degeneration in one monozygous twin in the initial disease stage. Cerebellum 10, 245–253.
Huber, K., et al., 2019. N-acetylaspartate pathway is nutrient responsive and coordinates lipid and energy metabolism in brown adipocytes. Biochim. Biophys. Acta, Mol. Cell Res. 1866, 337–348.
Huynh, D.P., et al., 2000. Nuclear localization or inclusion body formation of ataxin-2 are not necessary for SCA2 pathogenesis in mouse or human. Nat. Genet. 26, 44–50.
Jaeken, J., et al., 1984. Gamma-aminobutyric acid-transaminase deficiency: a newly recognized inborn error of neurotransmitter metabolism. Neuropediatrics 15, 165–169.
Kedersha, N., Anderson, P., 2007. Mammalian stress granules and processing bodies. Methods Enzymol. 431, 61–81.
Kedersha, N., et al., 2013. Stress granules and cell signaling: more than just a passing phase? Trends Biochem. Sci. 38, 494–506.
Kiehl, T.R., et al., 2006. Generation and characterization of Sca2 (ataxin-2) knockout mice. Biochem. Biophys. Res. Commun. 339, 17–24.
Koch, P., et al., 2011. Excitation-induced ataxin-3 aggregation in neurons from patients with Machado-Joseph disease. Nature 480, 543–546.
Lahut, S., et al., 2012. ATXN2 and its neighbouring gene SH2B3 are associated with increased ALS risk in the Turkish population. PLoS One 7, e42956.
Lastres-Becker, I., et al., 2008a. Insulin receptor and lipid metabolism pathology in ataxin-2 knock-out mice. Hum. Mol. Genet. 17, 1465–1481.
Lastres-Becker, I., et al., 2008b. Spinocerebellar ataxia 2 (SCA2). Cerebellum 7, 115–124.
Lastres-Becker, I., et al., 2016. Mammalian ataxin-2 modulates translation control at the pre-initiation complex via PI3K/mTOR and is induced by starvation. Biochim.

Biophys. Acta 1862, 1558–1569.
Lastres-Becker, I., et al., 2019. New alternative splicing variants of the *ATXN2* transcript. Neurological Research and Practice 1, 22.
Lee, T., et al., 2011. Ataxin-2 intermediate-length polyglutamine expansions in European ALS patients. Hum. Mol. Genet. 20, 1697–1700.
Lee, J.K., et al., 2015. Role of autophagy in the pathogenesis of amyotrophic lateral sclerosis. Biochim. Biophys. Acta 1852, 2517–2524.
Liu, J., et al., 2009. Deranged calcium signaling and neurodegeneration in spinocerebellar ataxia type 2. J. Neurosci. 29, 9148–9162.
Livak, K.J., Schmittgen, T.D., 2001. Analysis of relative gene expression data using real-time quantitative PCR and the 2(− Delta Delta C(T)) Method. Methods 25, 402–408.
Lu, Z.H., et al., 2004. N-Acetylaspartate synthase is bimodally expressed in microsomes and mitochondria of brain. Brain Res. Mol. Brain Res. 122, 71–78.
Mangiarini, L., et al., 1997. Instability of highly expanded CAG repeats in mice transgenic for the Huntington's disease mutation. Nat. Genet. 15, 197–200.
Mangus, D.A., et al., 1998. Pbp1p, a factor interacting with *Saccharomyces cerevisiae* poly (A)-binding protein, regulates polyadenylation. Mol. Cell. Biol. 18, 7383–7396.
Medrano-Montero, J., et al., 2018. Early cranial nerve dysfunction is correlated to altered facial morphology in spinocerebellar ataxia type 2. Investig. Discapacidad 7, 53–66.
Meierhofer, D., et al., 2016. Ataxin-2 (Atxn2)-knock-out mice show branched chain amino acids and fatty acids pathway alterations. Mol. Cell. Proteomics 15, 1728–1739.
Moffett, J.R., Namboodiri, M.A., 1995. Differential distribution of N-acetylaspartylglutamate and N-acetylaspartate immunoreactivities in rat forebrain. J. Neurocytol. 24, 409–433.
Nakken, O., et al., 2019. High BMI is associated with low ALS risk: a population-based study. Neurology 93, e424–e432.
Nonhoff, U., et al., 2007. Ataxin-2 interacts with the DEAD/H-box RNA helicase DDX6 and interferes with P-bodies and stress granules. Mol. Biol. Cell 18, 1385–1396.
Nonis, D., et al., 2008. Ataxin-2 associates with the endocytosis complex and affects EGF receptor trafficking. Cell. Signal. 20, 1725–1739.
Orozco Diaz, G., et al., 1990. Autosomal dominant cerebellar ataxia: clinical analysis of 263 patients from a homogeneous population in Holguin, Cuba. Neurology 40, 1369–1375.
Oz, G., et al., 2011. In vivo monitoring of recovery from neurodegeneration in conditional transgenic SCA1 mice. Exp. Neurol. 232, 290–298.
Oz, G., et al., 2015. Assessing recovery from neurodegeneration in spinocerebellar ataxia 1: comparison of in vivo magnetic resonance spectroscopy with motor testing, gene expression and histology. Neurobiol. Dis. 74, 158–166.
Paciorkowski, A.R., et al., 2011. Massive expansion of SCA2 with autonomic dysfunction, retinitis pigmentosa, and infantile spasms. Neurology 77, 1055–1060.
Park, H., et al., 2015. Parkinsonism in spinocerebellar ataxia. Biomed. Res. Int. 2015 125273.
Pfeffer, M., et al., 2017. Impact of Ataxin-2 knock out on circadian locomotor behavior and PER immunoreaction in the SCN of mice. Chronobiol. Int. 34, 129–137.
Pflieger, L.T., et al., 2017. Gene co-expression network analysis for identifying modules and functionally enriched pathways in SCA2. Hum. Mol. Genet. 26, 3069–3080.
Prokesch, A., et al., 2016. N-acetylaspartate catabolism determines cytosolic acetyl-CoA levels and histone acetylation in brown adipocytes. Sci. Rep. 6, 23723.
Pulst, S.M., et al., 1996. Moderate expansion of a normally biallelic trinucleotide repeat in spinocerebellar ataxia type 2. Nat. Genet. 14, 269–276.
Ragothaman, M., et al., 2004. Complex phenotypes in an Indian family with homozygous SCA2 mutations. Ann. Neurol. 55, 130–133.
Royland, J., et al., 1992. How much undernourishment is required to retard brain myelin development. Neurochem. Int. 21, 269–274.
Rub, U., et al., 2003a. Thalamic involvement in a spinocerebellar ataxia type 2 (SCA2) and a spinocerebellar ataxia type 3 (SCA3) patient, and its clinical relevance. Brain J. Neurol. 126, 2257–2272.
Rub, U., et al., 2003b. Anatomically based guidelines for systematic investigation of the central somatosensory system and their application to a spinocerebellar ataxia type 2 (SCA2) patient. Neuropathol. Appl. Neurobiol. 29, 418–433.
Rub, U., et al., 2004. Damage to the reticulotegmental nucleus of the pons in spinocerebellar ataxia type 1, 2, and 3. Neurology 63, 1258–1263.
Rub, U., et al., 2005a. Extended pathoanatomical studies point to a consistent affection of the thalamus in spinocerebellar ataxia type 2. Neuropathol. Appl. Neurobiol. 31, 127–140.
Rub, U., et al., 2005b. Spinocerebellar ataxias types 2 and 3: degeneration of the precerebellar nuclei isolates the three phylogenetically defined regions of the cerebellum. J. Neural Transm. 112, 1523–1545.
Rub, U., et al., 2006. Degeneration of ingestion-related brainstem nuclei in spinocerebellar ataxia type 2, 3, 6 and 7. Neuropathol. Appl. Neurobiol. 32, 635–649.
Rub, U., et al., 2007. Consistent affection of the central somatosensory system in spinocerebellar ataxia type 2 and type 3 and its significance for clinical symptoms and rehabilitative therapy. Brain Res. Rev. 53, 235–249.
Rub, U., et al., 2013. Clinical features, neurogenetics and neuropathology of the polyglutamine spinocerebellar ataxias type 1, 2, 3, 6 and 7. Prog. Neurobiol. 104, 38–66.
Satterfield, T.F., et al., 2002. A Drosophila homolog of the polyglutamine disease gene SCA2 is a dosage-sensitive regulator of actin filament formation. Genetics 162, 1687–1702.
Scherzed, W., et al., 2012. Pathoanatomy of cerebellar degeneration in spinocerebellar ataxia type 2 (SCA2) and type 3 (SCA3). Cerebellum 11, 749–760.
Scoles, D.R., 2017. Antisense oligonucleotide therapy for spinocerebellar ataxia type 2. Nature 544, 362–366.
Seidel, G., et al., 2017. Quantitative global proteomics of yeast PBP1 deletion mutants and their stress responses identifies glucose metabolism, mitochondrial, and stress granule changes. J. Proteome Res. 16, 504–515.
Sen, N.E., et al., 2016. Search for SCA2 blood RNA biomarkers highlights Ataxin-2 as strong modifier of the mitochondrial factor PINK1 levels. Neurobiol. Dis. 96, 115–126.
Sen, N.E., et al., 2017. PINK1 and Ataxin-2 as modifiers of growth. Oncotarget 8, 32382–32383.
Sudhakaran, I.P., et al., 2014. FMRP and Ataxin-2 function together in long-term olfactory habituation and neuronal translational control. Proc. Natl. Acad. Sci. U. S. A. 111, E99–E108.
Takahara, T., Maeda, T., 2012. Transient sequestration of TORC1 into stress granules during heat stress. Mol. Cell 47, 242–252.
Tuin, I., et al., 2006. Stages of sleep pathology in spinocerebellar ataxia type 2 (SCA2). Neurology 67, 1966–1972.
van de Loo, S., et al., 2009. Ataxin-2 associates with rough endoplasmic reticulum. Exp. Neurol. 215, 110–118.
Velazquez-Perez, L., et al., 2001. Hereditary ataxias in Cuba. Historical, epidemiological, clinical, electrophysiological and quantitative neurological features. Rev. Neurol. 32, 71–76.
Velazquez-Perez, L., et al., 2004. Saccade velocity is controlled by polyglutamine size in spinocerebellar ataxia 2. Ann. Neurol. 56, 444–447.
Velazquez-Perez, L., et al., 2009. Saccade velocity is reduced in presymptomatic spinocerebellar ataxia type 2. Clin. Neurophysiol. 120, 632–635.
Velazquez-Perez, L., et al., 2014. Progression of early features of spinocerebellar ataxia type 2 in individuals at risk: a longitudinal study. Lancet Neurol. 13, 482–489.
Velazquez-Perez, L., et al., 2016. Abnormal corticospinal tract function and motor cortex excitability in non-ataxic SCA2 mutation carriers: a TMS study. Clin. Neurophysiol. 127, 2713–2719.
Velazquez-Perez, L., et al., 2017a. Early corticospinal tract damage in prodromal SCA2 revealed by EEG-EMG and EMG-EMG coherence. Clin. Neurophysiol. 128, 2493–2502.
Velazquez-Perez, L.C., et al., 2017b. Spinocerebellar Ataxia type 2: Clinicogenetic aspects, mechanistic insights, and management approaches. Front. Neurol. 8, 472.
Vinther-Jensen, T., et al., 2013. Germ-line CAG repeat instability causes extreme CAG repeat expansion with infantile-onset spinocerebellar ataxia type 2. Eur. J. Hum. Genet. 21, 626–629.
Wang, X., Chen, X.J., 2015. A cytosolic network suppressing mitochondria-mediated proteostatic stress and cell death. Nature 524, 481–484.
Wang, P.S., et al., 2012. Association between proton magnetic resonance spectroscopy measurements and CAG repeat number in patients with spinocerebellar ataxias 2, 3, or 6. PLoS One 7, e47479.
Wills, A.M., et al., 2014. Hypercaloric enteral nutrition in patients with amyotrophic lateral sclerosis: a randomised, double-blind, placebo-controlled phase 2 trial. Lancet 383, 2065–2072.
Yang, Y.S., et al., 2019. Yeast Ataxin-2 forms an intracellular condensate required for the inhibition of TORC1 signaling during respiratory growth. Cell 177 697–710 e17.
Zhang, H.H., et al., 2009. Insulin stimulates adipogenesis through the Akt-TSC2-mTORC1 pathway. PLoS One 4, e6189.